Truncating Tau Reveals Different Pathophysiological Actions of Oligomers in Single Neurons

Emily Hill[1*], Thomas K. Karikari[2], Juan Lantero Rodriguez[2], Henrik Zetterberg[2,3,4,5], Kaj Blennow[2,3], Magnus J Richardson[6], Mark J Wall[1*]

[1]School of Life Sciences, University of Warwick, Coventry CV4 7AL, United Kingdom

[2]Department of Psychiatry and Neurochemistry, Institute of Neuroscience and Physiology, University of Gothenburg, SE-43180 Mölndal, Sweden.

[3]Clinical Neurochemistry Laboratory, Sahlgrenska University Hospital, SE-43180 Mölndal, Sweden.

[4]UK Dementia Research Institute at UCL, London WC1E 6BT, United Kingdom

[5]Department of Neurodegenerative Disease, UCL Institute of Neurology, London WC1E 6BT, United Kingdom

[6]Institute of Mathematics, University of Warwick, Coventry CV4 7AL, United Kingdom

*Authors for correspondence: Emily Hill E.hill.2@warwick.ac.uk and Mark Wall Mark.wall@warwick.ac.uk

Abstract

Tau protein is involved in maintaining the structural integrity of neurons. In tauopathies, including Alzheimer's disease, tau forms oligomers, which can modulate neuronal function. Previously the introduction of oligomeric full-length human tau (aa 1-441; FL-oTau) into pyramidal neurons decreased whole-cell conductance, increased excitability and changed the action potential (AP) waveform. Introducing N-terminally truncated tau (aa 124-441; C^{FRAG}) removed the effects on the AP waveform and input resistance but the increase in excitability remained. A hyperpolarising shift in spike threshold underlies this increase in excitability. The N-terminal fragment (aa 1-123; N^{FRAG}) markedly increased input resistance and changed the AP waveform. Lower concentrations of N^{FRAG} only changed the AP waveform. Thus the two truncations can recapitulate the effects of FL-oTau. To investigate underlying mechanisms, we recorded sodium currents and found that FL-oTau lowers the activation voltage and reduced the maximal conductance, consistent with the lower spike threshold and reduction in AP amplitude

Graphic abstract

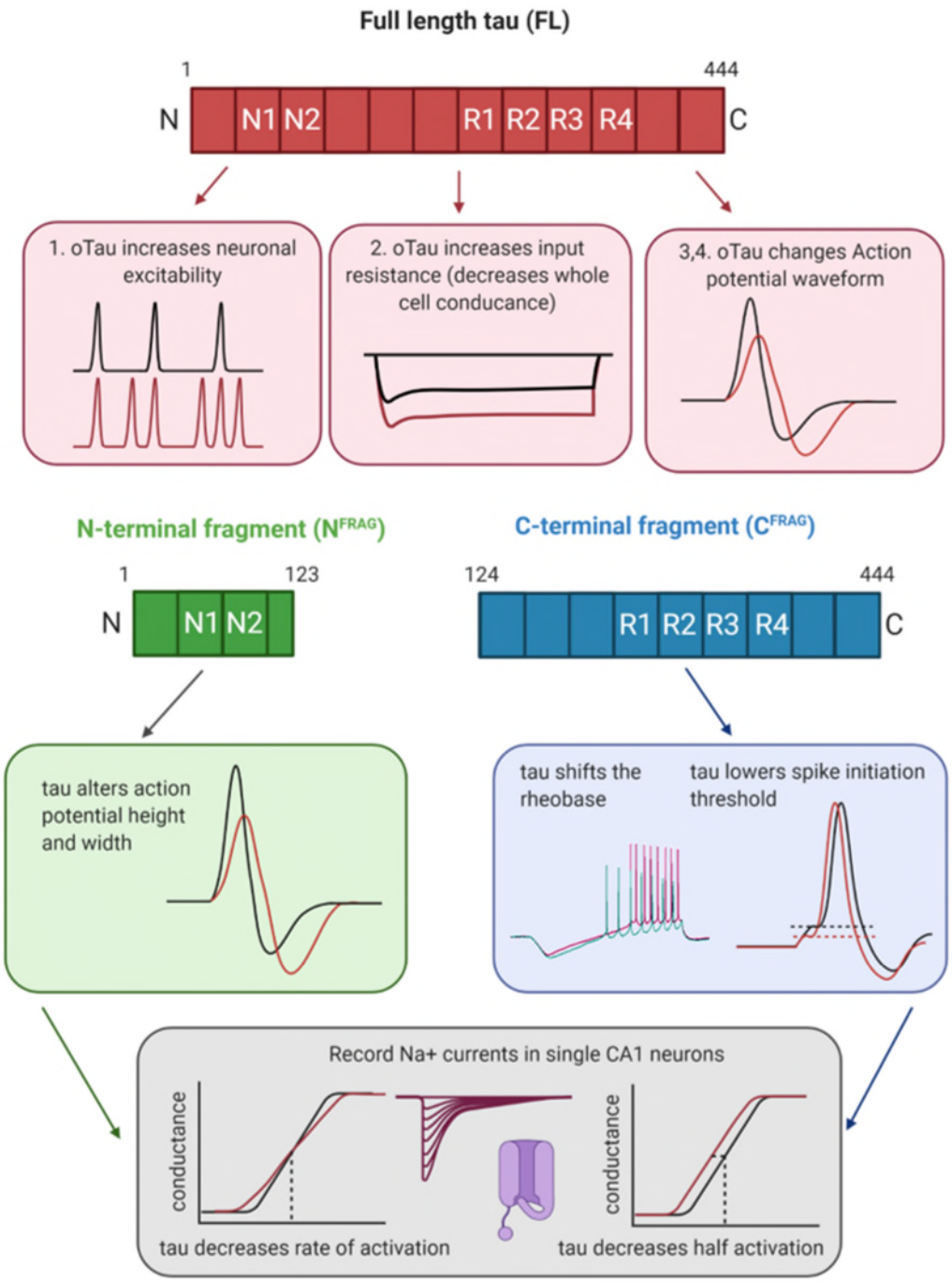

Key Words (4-6 words)

Tau oligomers, Alzheimer's disease, Electrophysiology, Sodium currents

Introduction

Tau is a microtubule-associated protein which can modify neuronal morphology, vesicle transport and trafficking (Brandt and Lee, 1993; Tracy and Gan, 2018). Tau dysfunction contributes to diseases, termed tauopathies, either as the primary causative agent (*e.g.*, Pick's disease) or as a component of the neuropathology (*e.g.*, Alzheimer's disease, AD). Tauopathies have varying histopathological and clinical presentations and are often distinguished by the ultrastructure of the tau aggregates (Dickson et al., 2011; Rademakers et al., 2012). In AD, abnormally phosphorylated tau dissociates from microtubules and aggregates to form oligomers and fibrils, accumulating in the soma-dendritic compartment (Köpke et al., 1993). Tau can further aggregate to form neurofibrillary tangles (NFTs), whose abundance correlates with disease progression (Avila et al., 2006; Maeda et al., 2006). However, it appears that the soluble tau oligomers (oTau) are the most bioactive, in terms of disrupting neuronal function. Indeed, the toxic effects of tau oligomers can occur in the absence of NFT pathology (Andorfer et al., 2003; Cowan et al., 2010; Yoshiyama et al., 2007). Although the toxicity of oTau is now well established, the mechanistic basis of oTau actions on neuronal function is poorly understood.

Electrophysiological studies have revealed several pathological mechanisms of oTau, including alterations in neuronal excitability and short- and long-term synaptic plasticity (Hill et al., 2019; Hoover et al., 2010; Mondragón-Rodríguez et al., 2018; Puzzo et al., 2017). Viral introduction and transgenic models are commonly used to explore the role of oTau (Andorfer et al., 2003; Cowan et al., 2010; Yoshiyama et al., 2007). While these methods generate valuable data, they provide little information on the concentration and structural conformations of oTau that are responsible for the neurotoxic effects. For other approaches, such as the extracellular application of oTau to tissue or cell cultures (Acquarone et al., 2019; Fá et al., 2016; Ondrejcak et al., 2018), cellular uptake may be the liming step, reducing the observed toxicity. Moreover, it is not possible to target oligomers to either pre- or post-synaptic neurons and homeostatic adaptation may occur.

To address these limitations, whole-cell patch-clamp recording has recently been used to introduce oTau into single neurons and has enabled specific targeting into either pre- or post-synaptic cells (Hill et al., 2019). This approach requires small amounts of oligomers, each cell acts as its own control and electrophysiological alterations can be observed in real time. Furthermore, direct comparisons can be made between different concentrations and structural conformations of the oTau introduced (Hill et al., 2020, 2019; Kaufmann et al., 2016).

Previously full-length (FL, prepared from full-length human tau 1-441) oTau was shown to modify excitability, input resistance and action potential waveform (Hill et al 2019). We reasoned that specific truncations of tau may allow these effects to be dissected apart, identifying underlying mechanisms and which parts of the molecule causes which effect. We therefore created truncated versions of tau informed by a physiologically-relevant truncation at amino acid 123 that was recently discovered in AD patients (Cicognola et al., 2019). We used oligomers formed from tau lacking the N-terminal region (aa 124-444; C^{FRAG}) and soluble aggregates of the non-oligomer forming N-terminal fragment (aa 1-123;

N^{FRAG}). Using these tau constructs, we have identified specific mechanisms underlying the changes to excitability, conductance and AP waveform.

Results

Structural characterisation of the tau samples

We employed a validated method to generate non-fibrillar soluble tau aggregates without the use of aggregation-inducing factors such as heparin (Hill et al., 2019; Karikari et al., 2019b, 2019a). Incubating all three tau samples (FL oligomers, C^{FRAG} oligomers, N^{FRAG} soluble aggregates; Fig 1A) at room temperature overnight led to the formation of small soluble aggregates, as shown by negative-stain transmission electron microscopy (TEM). However, there were structural differences in the aggregate conformers; C^{FRAG} tau formed granular shaped oligomeric aggregates similar to those of FL-tau (Fig. 1B and Hill et al., 2019; Karikari et al., 2019a, 2019b). Conversely, N^{FRAG} tau formed amorphous, irregular-shaped, non-amyloidogenic aggregates, in agreement with Lapointe et al., (2009). For each variant, monomeric controls (incubated for the same duration but at 4 ˚C) did not form aggregates (Fig 1B).

Using oligomeric C^{FRAG} to separate effects on whole-cell conductance, neuronal excitability and action potential waveform

We first compared the effects of C^{FRAG} oTau to FL oTau (vehicle as control). There was no significant difference in the electrophysiological parameters at time 0 (whole-cell breakthrough), therefore, the initial quality of recordings and neuronal properties were comparable. In control neurons there were no changes to any measured parameters (Fig 2; Table 1). There were also no changes to the resting membrane potential (RMP) for any of the experimental conditions (Fig 2A, B; Table 1). FL-oTau had comparable effects to those reported in (Hill *et al* 2019): increasing input resistance (Rin), increasing neuronal excitability and changing the AP waveform (reduced amplitude and increased width). These effects were specific to oligomers, with monomeric tau having no significant effects. FL oTau increased neuronal excitability, which we assumed was a result of increased Rin (Fig 2C, D, E). Surprisingly, although C^{FRAG} oTau had no effect on Rin (Fig 2C), it still significantly increased firing rate suggesting that the effects on neuronal excitability can occur independently of changes in Rin (Fig 2C-E). In contrast to FL-oTau which (in agreement with Hill *et al*., 2019) significantly alters AP width and amplitude over 40 minutes of recording, introduction of C^{FRAG} tau had no effect on the AP waveform (Fig 2D-G). Thus, the effects of FL oTau on AP waveform could either be a direct result of the removed N-terminal sequence or could result from a structure specificity of the oligomers, which probably differs following truncation.

The increase in neuronal excitability is confirmed by a reduction in rheobase current.

To evaluate the effects on neuronal excitability in more detail, we examined the rheobase: the minimal current required to elicit an AP. There was no significant difference in rheobase in control vs FL or C^{FRAG} oTau injected neurons at time 0 (Table 1, Figure 3). In control neurons, there was no significant difference in the rheobase current over the duration of the recording. However, when either FL or C^{FRAG} oTau were introduced, the rheobase was significantly reduced (reflecting an increase in excitability,

Table 1, Figure 3). This data is also consistent with the effect on the frequency of APs in response to fluctuating noisy current traces (Figure 2F,G).

C^{FRAG} tau oligomers reduce the current needed to elicit APs

We hypothesized that the decrease in rheobase current might be due to a smaller difference between the RMP and spike initiation threshold. Since there is no change in RMP, this could only occur if there was a hyperpolarising shift in spike initiation threshold (Δ_T). The dynamic IV method (Badel et al., 2008a, 2008b; Harrison et al., 2015) provides a method to accurately parameterise neurons including Δ_T (see methods). In Hill et al., (2019), it was not possible to map changes in neuronal parameters over time as the dynamic IV method is not very effective if there are significant changes in the AP waveform. However, as C^{FRAG} oTau has no effect on the AP waveform, it is possible to use this method to measure Δ_T. There was no significant difference between the Δ_T in control vs C^{FRAG} neurons at time 0. In control neurons, there was no significant difference in Δ_T, whereas for neurons where C^{FRAG} oTau was introduced, Δ_T was significantly reduced (more negative) at 40 minutes compared to 0 minutes. Although the reduction in Δ_T was only ~4 mV, across a network this would cause a significant to shift in excitability. We also noted an increase in spike onset sharpness which is a measure of how sharp the voltage range is within which a spike starts to initiate, as well as how sharply the spike begins to rise (sharper DIV curve). In control neurons, there was no significant difference in spike onset over the duration of the recording, whereas for neurons where C^{FRAG} oTau was introduced, the onset was increased (steeper, reflecting increased excitability). It can be noted that though the spike-onset range was broader at 40 mins, this change (unlike for the spike threshold parameter V_T) had no significant effect on the excitation or firing rate (see Fig. 4D).

N^{FRAG} aggregate introduction generates a rapid onset increase in input resistance

As C^{FRAG} oTau did not replicate the changes to Rin and AP waveform observed with FL oTau, we next introduced N^{FRAG} tau and measured changes to neuronal parameters to determine if this fragment of tau was responsible. Unexpectedly, in preliminary experiments we observed a large increase in input resistance by N^{FRAG} oTau within the first 5 minutes of recording (Fig 5A). It has previously been shown that FL oTau neither aggregates in the end of the pipette tip nor impedes voltage measurements through re-patching experiments (Hill et al., 2019). However, this rapid change could be due to N^{FRAG} forming aggregates close to the introduction site in the soma and reducing the apparent electrotonic size of the soma. By fitting the voltage step (exponential) we extracted the time constant and used this to calculate cellular capacitance using the following equation:

$$Time\ constant\ (T) = Input\ resistance\ (R_{in})\ x\ Capacitance\ (C)$$

By 5 mins, the time constant was significantly reduced, reflecting a change in whole-cell capacitance.

To test the possibility that this rapid change to whole-cell resistance and capacitance could be due to the aggregation of the N^{FRAG} tau in the soma impeding current flow, we performed a subset of experiments where two simultaneous whole-cell patch clamp recordings were made to the same CA1 pyramidal neuron (Fig 5B; see methods). In turn we injected a 200 pA hyperpolarising (1s) step to elicit a voltage response in both the pipette that we injected the current with, but also from the second "recording only" pipette (Fig 5C). As the current needs to travel to the 'recording only' pipette, the voltage response was always slightly smaller than the response measured by the 'inject and record' pipette. In cells where both pipettes were filled with vehicle, there was no change in the relative amplitude of the responses ($V_{rec}/V_{rec+inject}$) between 0 mins (whole-cell breakthrough) and 5 mins (Fig 5D). However, when N^{FRAG} tau was introduced in the 'inject and record pipette', the same large rapid increase in input resistance (as in Fig 5A) was observed. This was not reflected in an increase in the amplitude of the voltage step as measured by the second 'recording only' pipette (Fig 5E, F). Thus, the results confirm that at this concentration of N^{FRAG} oTau, they must be accumulating in the soma, impeding the flow of current between the two pipettes, resulting in an 'artificial' increase in input resistance and decrease in the observed capacitance due to the cell appearing electronically smaller.

Tau-mediated changes to action-potential waveform are independent of aggregate form

We have demonstrated that the FL-oTau mediated increase in Rin and changes to AP waveform occurred at later time points than we observed with N^{FRAG} tau. This may be because the FL o-Tau does not aggregate as effectively as N^{FRAG} tau and thus takes longer to have effects. Thus, to examine the effects of N^{FRAG} tau in more detail we used a lower concentration (133 nM) which will mimic the slower effects of FL oTau. There were no effects of 133 nM N^{FRAG} oTau introduction on RMP, Rin, firing rate or rheobase current (Fig 6A-D). However, the significant changes to AP waveform (increased width and decreased amplitude) that were observed both in (Hill et al., 2019) and with FL oTau in this study were also observed with 133 nM N^{FRAG} tau aggregates (Fig 6E-G). This was unexpected as the N-terminal fragment will form structurally different aggregates to FL tau oligomers. We repeated the experiments with the monomeric version of N^{FRAG} tau and found no changes in RMP Rin, firing rate or rheobase current (Fig 6A-D). However, a comparable change to AP waveform was observed (Fig 6E-G). Given that the oTau-induced changes to AP waveform that occur with full length tau (Hill et al., 2019) also occurred with the N-terminal fragment (N^{FRAG}), both as a monomer and an oligomer, it is likely that there is a sequence within the 1-123 amino acid region that directly interacts with a cellular component rather than being an effect of the quaternary structure of the aggregates.

oTau alters somatic voltage gated sodium channel half activation and slows the rate of activation

Having demonstrated changes to AP waveform and a shift in Δ_T, making the neurons more excitable, we next investigated whether these changes were mediated by interactions of tau with voltage gated sodium channels. Recording sodium channel currents in hippocampal neurons in acute brain slices is challenging due to problems with space clamp, given the size of the neurons and the large amplitude and speed of the currents. One way to effectively clamp the currents, is to electronically isolate the soma. We followed the protocol outlined in Milescu et al., (2010), using a short depolarising pre-pulse to inactivate the axonal sodium channels, leaving only the somatic channels to be activated (see methods). It was then possible to achieve reasonable voltage clamp (Fig 7A). Normalised conductance's were plotted against voltage and fitted with a Boltzmann function. The fit (Fig 7B, C) was used to extract the half activation voltage and the rate constant of activation (indicative of the rate of rise in conductance relative to change in voltage). The half activation was stable in control recordings, whereas in neurons that had FL-oTau introduced, by 20 minutes the half activation had shifted significantly in a negative direction to activate ~ 4mV earlier, reflective of an increase in excitability (Fig 7). This could account for the change in Δ_T that was observed with C^{FRAG} oTau. We also extracted the rate constant of activation; a smaller rate constant would indicate a steeper relationship between conductance and voltage. The rate constant of activation was stable in control, whereas in neurons that had FL-oTau introduced, by 20 minutes it had increased significantly (shallower slope, reflective of a flatter relationship to voltage). This change could explain the slowing of the AP rising phase observed in (Hill et al., 2019) and in this study.

We then implemented a simplified model of the neuronal AP with general applicability (Hodgkin and Huxley, 1952) to evaluate whether the conductance changes mediated by FL-oTau could feasibly underly the changes we observed in AP waveform. Our experimental voltage gated sodium current recordings showed that FL-oTau mediates a reduction of $\bar{g}_{Na}$ to by two thirds of the value at 0 minutes after 20 minutes (7F-I). Therefore, we first simulated an AP with $\bar{g}_{Na} = 120\ mS/cm^2$ (Hodgkin and Huxley, 1952, Figure 7J, red) and then again with $\bar{g}_{Na} = 40\ mS/cm^2$ (Figure 7J, red trace). We found that this reduction in $\bar{g}_{Na}$ matches the experimental phenotype well (the changes in AP amplitude and speed of rise to threshold; Figure 7K).

Discussion

In Alzheimer's disease (AD) and in other tauopathies, tau aggregates into small soluble toxic oligomers, a process that precedes the formation of large insoluble aggregates (NFTs). In AD, NFTs and amyloid-β plaques are the characteristic hallmarks of the disease with post-mortem confirmation of both NFTs and plaques required for definitive diagnosis (Braak and Braak, 1991; Avila et al., 2006; Maeda et al., 2006). Many studies have shown that the small soluble aggregates (oligomers) formed early in the aggregation pathway are much more bioactive than NFTs pathology (Andorfer et al., 2003; Cowan et al., 2010; Yoshiyama et al., 2007). These findings have led to the targeting of oligomers to reduce tau cytotoxicity in disease models and in AD patients. However, the mechanisms of how these oligomers produce neuronal dysfunction are still not fully defined. Here, we have used specific truncations to dissect apart the actions of full length (FL) oTau. We have used oligomers formed from N-terminal truncated tau (aa 124-444; C^{FRAG}) and soluble aggregates of the non-oligomer forming N-terminal fragment (aa 1-123; N^{FRAG}).

C^{FRAG} tau produces oligomers that increase excitability by changing spike threshold

The N-terminal truncation (C^{FRAG}) at position 123, has been identified as a major N-terminal cleavage site in human CSF (Cicognola et al., 2019) and a truncated tau construct at a nearby position has been used to study effects on synaptic transmission (Zhou et al., 2017). We found that C^{FRAG} oTau did not replicate the effects on action potential (AP) kinetics or input resistance (Rin) that were observed with FL oTau but did still increase excitability. This excitability increase is mediated by a reduction in the minimum current required to elicit an AP. Using the dynamic IV protocol we found that C^{FRAG} oTau reduces spike threshold by ~ 4mV. Since there was no change in the resting membrane potential, the difference between spike threshold and resting potential was reduced, increasing the likelihood of firing. To confirm this observation, the parameters extracted from the dynamic IV curve at 0 minutes were used to simulate voltage responses using the exponential integrate and fire model (Badel et al., 2008b; Fourcaud-Trocmé et al., 2003; Harrison et al., 2015). The control firing rate was comparable to experimental values. A reduction in the spike threshold by the experimentally observed reduction (4 mV), was sufficient to increase the firing rate to comparable experimental values with C^{FRAG} oTau. Thus, it is feasible for a change in spike threshold (without any change in Rin) to mediate the observed changes in neuronal excitability by C^{FRAG} oTau.

N^{FRAG} tau aggregates change input resistance

We then investigated the tau fragment that was removed to generate C^{FRAG} (aa 1-123; N^{FRAG}). This fragment (N^{FRAG}) makes up a large proportion of N-terminal tau species found in human CSF, and it therefore could represent a marker of tau metabolism (Cicognola et al., 2019). N^{FRAG} does form aggregates but these differ from the FL-oTau oligomers. When N^{FRAG} was introduced into neurons at equivalent concentrations to FL oTau (444 nM), it produced a rapid increase in Rin, reduced AP amplitude and slowed AP kinetics. These effects occurred within ~5 minutes. Through measurements of the cell time constant we found that the apparent capacitance was significantly decreased. This led us to hypothesise that N^{FRAG} was inferring with current flow, making the neuron electrotonically smaller.

By making simultaneous dual patch clamp recordings from the soma of a single neuron, we found that although Rin was significantly increased, the current flow between the electrodes had significantly decreased. This is consistent with N^{FRAG} tau aggregating in the soma and impeding current flow across the cell.

N^{FRAG} tau aggregates change AP amplitude and width at low concentrations

Introducing N^{FRAG} at lower concentrations (133 nM) changed AP amplitude and width without increasing Rin or changing cell capacitance. Thus, the changes in AP waveform are not simply due to increased filtering. Surprisingly, N^{FRAG} monomers produced comparable changes to APs. Thus, the effects of N^{FRAG} are unrelated to its quaternary structure and instead maybe associated with a specific sequence within N^{FRAG} and FL oTau. Given the nature of the changes in AP waveform we hypothesised that tau might be interacting with voltage-gated sodium channels and altering their function.

FL-oTau alters voltage-gated sodium currents

Changes in AP kinetics and amplitude can be measured using whole cell voltage clamp (Hodgkin and Huxley, 1952). Recording sodium currents from neurons in slices is challenging due to space clamp problems and the large amplitude and rapid rise of currents (Rall and Segev, 1985; Spruston et al., 1993). A large proportion of sodium channels are clustered in the axon initial segment (AIS, Castelli et al., 2007; Kole et al., 2008; Royeck et al., 2008), and their activation voltage can differ significantly from that at the soma (Kole et al., 2008; Stuart et al., 1997). Thus, these electrotonically remote sodium channels will generate unclamped currents, which prevent the measurement of controlled responses. To counteract this problem, most measurements of sodium channel currents are performed in nucleated patches, dissociated or cultured neurons or in cell lines. However, these are less relevant physiologically relevant because the distribution, density and expression pattern of channels will be different from what is found in situ. We adapted a protocol (Milescu et al., 2010) to make controlled voltage clamp recordings in acute slices. A pre-pulse elicits an uncontrolled voltage response which activates axonal but not somatic sodium channels. As the axonal channels are inactivated, only the sodium channels in the soma contribute to the actual recorded current, allowing for finely controlled voltage clamp of the sodium currents. This protocol also required a number of other steps to produce clamp of isolated sodium channel currents including changing the Na^+ concentration inside and outside of the neuron, performing recordings at room temperature and replacing the calcium ions with cobalt to block voltage gated calcium channels (Puopolo et al., 2007).

There are four subtypes of voltage-gated sodium channel present in the mammalian central nervous system, NaV 1.1,1.2,1.3,1.6 (de Lera Ruiz and Kraus, 2015). At the AIS of CA1 pyramidal neurons, NaV1.1, NaV1.2, and NaV1.6 channels have been identified (Akin et al., 2015; Garrido et al., 2003; Van Wart et al., 2007). NaV1.6 is highly abundant and has a more hyperpolarized voltage of activation compared with the other a sodium channel isoforms, contributing to the lower activation threshold (Royeck et al., 2008). The sodium channels in the AIS probably contribute little to the clamped currents and this is a possible limitation of the technique. However NaV1.6 is also expressed in the soma,

although at less abundance than at the AIS (Lorincz and Nusser, 2010). Despite this, we have made measurements of sodium channel currents in acute slices which is more physiologically realistic than recombinant channels in cell lines.

FL-oTau had three effects on sodium channel currents: Firstly, the half activation was reduced, reflecting the increase in neuronal excitability, consistent with the effects of C^{FRAG}. Secondly, the rate of activation was reduced, underlying the slower AP rise, consistent with the effects of N^{FRAG} introduction. Finally, FL-oTau reduced $\bar{g}_{Na}$ (maximum sodium conductance) by ~ two thirds. To investigate the effects that this would have on the AP, we implemented a simplified AP model (Hodgkin and Huxley, 1952). Reducing $\bar{g}_{Na}$ had effects that matched the experimental data (reducing AP amplitude and increasing rise to threshold). Thus, this reduction in conductance alone could account for the changes in AP waveform that were observed experimentally.

From the unnormalized conductance plots, we noticed that the rate of conductance increase appeared faster for FL-oTau despite $\bar{g}_{Na}$ being reduced (Figure 7I). We therefore modelled the initial rise of the sodium current using the same approach (Fourcaud-Trocmé et al., 2003) to derive the original model:

$$I_{Na} = (E_{Na} - E_{rest}) * g1 * e^{(\frac{V-V1}{\Delta T})}$$

Where $g1$ is 1 nS and V1 is the voltage where the conductance is 1 nS. For FL-oTau introduced cells, ΔT was calculated to be stable ~2.65 mV for 0 mins and 20 mins but $V1$ varied over time. At 0 mins, $V1$ = -32 mV and by 20 mins, $V1$ = -36 mV, demonstrating that a sodium conductance of 1 nS is achieved at a much lower voltage, thus the cell is more excitable (despite the peak sodium conductance being lower, Figure 7I). In the EIF model, the sodium current is modelled as:

$$\Delta T * gL * e^{(\frac{V-VT}{\Delta T})}$$

and comparing this with the equation for I_{Na} we get:

$$VT = V1 + \Delta T * \log(gL * \frac{\Delta T}{g1} * (E_{Na} - E_{rest})$$

Empirically, the first term V_1 on the right-hand-side is dependent on parameters that change between 0 mins and 40 mins, whereas the second term does not change significantly between these time steps. Hence the modelling predicts that the change in the action-potential threshold parameter V_T is largely due to changes in V_1 which is the voltage at which the sodium current is 1nS. The I_{Na} experiments predict that the difference in VT at 0 and 40 mins is 4 mV, which fits exactly with the excitability phenotype modelled using C^{FRAG}. Despite the differences in temperature for these recordings, two independent methodologies both suggest that the tau-mediated shift in excitability comes from a lowering of the action-potential threshold (rather than input resistance changes) and that this change is mediated via a lowering of the sodium current activation.

It is surprising to note that the difference in sodium conductance at 0 minutes and 20 minutes with FL-oTau is dependent on voltage, at low voltages the conductance is bigger at 20 mins in FL-oTau but at high voltages it is lower at 20 mins in o-Tau, thus, the effects are non-monotonic. Globally it appears that there is a lower maximal conductance at 20 mins (and therefore AP height is reduced), but there is a small region at low voltages where the conductance is higher for FL-oTau, which means the model is more excitable. This means the profile of the I_{Na} activation has been changed by oTau; it is not just an issue of different maximal conductance magnitudes.

The simplest explanation for these changes to sodium conductance is that a specific N^{FRAG} tau sequence binds to the sodium channel. The mammalian sodium channel is a molecular complex of an ~2000 amino acid α-subunit, which contains the pore and drug interaction sites, and smaller β-subunits, which modulate membrane expression (Catterall, 2000; Patino and Isom, 2010). The α-subunit is divided into 4 domains each with 6 segments (S1-S6). S1-4 form the voltage sensing domain (Kontis et al., 1997) and S5-6 form the pore forming domain. Upon depolarisation, S6 segments move leading to channel opening via the P-loop between S5 and S6 which forms the channel pore (de Lera Ruiz and Kraus, 2015; Fozzard et al., 2011). The S4 segments contain a high proportion of positively charged amino acid residues, making it responsive to changes in membrane potential (Bezanilla, 2000). It is interesting to speculate on where the tau oligomers could bind to sodium channels, changing the coupling between depolarisation and pore opening. Many studies have shown that changes in the S4 segments, associated linkers and cytoplasmic loops can all change the activation of the channels (de Lera Ruiz and Kraus, 2015; Fozzard et al., 2011).

Conclusions

This work has shown that by modifying the tau molecule it is possible to dissect apart the multiple effects it has on neuronal function (Table 2) and identify a molecular target that tau binds to. This not only provides information about the mechanisms of action of tau but also raises interesting possibilities. Since the truncations used in this study have been found in the CSF of AD patients, then the effects of tau will depend on the mixture of these molecules inside neurons. Thus, if tau is primarily present as the C^{FRAG} then it will affect excitability and not change AP waveform. However, if the N^{FRAG} accumulates in the soma it will have large effects on neuronal integration and AP waveform. Also are these effects specific to only some sodium channel isoforms effecting some neurons more than others.

References

1. Acquarone, E., Argyrousi, E.K., van den Berg, M., Gulisano, W., Fà, M., Staniszewski, A., Calcagno, E., Zuccarello, E., D'Adamio, L., Deng, S.-X., Puzzo, D., Arancio, O., Fiorito, J., 2019. Synaptic and memory dysfunction induced by tau oligomers is rescued by up-regulation of the nitric oxide cascade. Mol. Neurodegener. 14, 26. https://doi.org/10.1186/s13024-019-0326-4

2. Akin, E.J., Solé, L., Dib-Hajj, S.D., Waxman, S.G., Tamkun, M.M., 2015. Preferential Targeting of Nav1.6 Voltage-Gated Na+ Channels to the Axon Initial Segment during Development. PLoS ONE 10. https://doi.org/10.1371/journal.pone.0124397
3. Andorfer, C., Kress, Y., Espinoza, M., de Silva, R., Tucker, K.L., Barde, Y.-A., Duff, K., Davies, P., 2003. Hyperphosphorylation and aggregation of tau in mice expressing normal human tau isoforms. J. Neurochem. 86, 582–590. https://doi.org/10.1046/j.1471-4159.2003.01879.x
4. Avila, J., Santa-María, I., Pérez, M., Hernández, F., Moreno, F., 2006. Tau phosphorylation, aggregation, and cell toxicity. J. Biomed. Biotechnol. 2006, 74539. https://doi.org/10.1155/JBB/2006/74539
5. Badel, L., Lefort, S., Berger, T.K., Petersen, C.C.H., Gerstner, W., Richardson, M.J.E., 2008a. Extracting non-linear integrate-and-fire models from experimental data using dynamic I–V curves. Biol. Cybern. 99, 361–370. https://doi.org/10.1007/s00422-008-0259-4
6. Badel, L., Lefort, S., Brette, R., Petersen, C.C.H., Gerstner, W., Richardson, M.J.E., 2008b. Dynamic *I-V* Curves Are Reliable Predictors of Naturalistic Pyramidal-Neuron Voltage Traces. J. Neurophysiol. 99, 656–666. https://doi.org/10.1152/jn.01107.2007
7. Bezanilla, F., 2000. The Voltage Sensor in Voltage-Dependent Ion Channels. Physiol. Rev. 80, 555–592. https://doi.org/10.1152/physrev.2000.80.2.555
8. Bezanson, J., Edelman, A., Karpinski, S., Shah, V.B., 2017. Julia: A Fresh Approach to Numerical Computing. SIAM Rev. 59, 65–98. https://doi.org/10.1137/141000671
9. Brandt, R., Lee, G., 1993. Functional organization of microtubule-associated protein tau. Identification of regions which affect microtubule growth, nucleation, and bundle formation in vitro. J. Biol. Chem. 268, 3414–3419.
10. Castelli, L., Biella, G., Toselli, M., Magistretti, J., 2007. Resurgent Na+ current in pyramidal neurones of rat perirhinal cortex: axonal location of channels and contribution to depolarizing drive during repetitive firing. J. Physiol. 582, 1179–1193. https://doi.org/10.1113/jphysiol.2007.135350
11. Cicognola, C., Brinkmalm, G., Wahlgren, J., Portelius, E., Gobom, J., Cullen, N.C., Hansson, O., Parnetti, L., Constantinescu, R., Wildsmith, K., Chen, H.-H., Beach, T.G., Lashley, T., Zetterberg, H., Blennow, K., Höglund, K., 2019. Novel tau fragments in cerebrospinal fluid: relation to tangle pathology and cognitive decline in Alzheimer's disease. Acta Neuropathol. (Berl.) 137, 279–296. https://doi.org/10.1007/s00401-018-1948-2
12. Cowan, C.M., Chee, F., Shepherd, D., Mudher, A., 2010. Disruption of neuronal function by soluble hyperphosphorylated tau in a Drosophila model of tauopathy. Biochem. Soc. Trans. 38, 564–570. https://doi.org/10.1042/BST0380564
13. de Lera Ruiz, M., Kraus, R.L., 2015. Voltage-Gated Sodium Channels: Structure, Function, Pharmacology, and Clinical Indications. J. Med. Chem. 58, 7093–7118. https://doi.org/10.1021/jm501981g
14. Dickson, D.W., Kouri, N., Murray, M.E., Josephs, K.A., 2011. Neuropathology of frontotemporal lobar degeneration-tau (FTLD-tau). J. Mol. Neurosci. MN 45, 384–389. https://doi.org/10.1007/s12031-011-9589-0

15. Fá, M., Puzzo, D., Piacentini, R., Staniszewski, A., Zhang, H., Baltrons, M.A., Li Puma, D.D., Chatterjee, I., Li, J., Saeed, F., Berman, H.L., Ripoli, C., Gulisano, W., Gonzalez, J., Tian, H., Costa, J.A., Lopez, P., Davidowitz, E., Yu, W.H., Haroutunian, V., Brown, L.M., Palmeri, A., Sigurdsson, E.M., Duff, K.E., Teich, A.F., Honig, L.S., Sierks, M., Moe, J.G., D'Adamio, L., Grassi, C., Kanaan, N.M., Fraser, P.E., Arancio, O., 2016. Extracellular Tau Oligomers Produce An Immediate Impairment of LTP and Memory. Sci. Rep. 6, 19393. https://doi.org/10.1038/srep19393
16. Fourcaud-Trocmé, N., Hansel, D., Vreeswijk, C. van, Brunel, N., 2003. How Spike Generation Mechanisms Determine the Neuronal Response to Fluctuating Inputs. J. Neurosci. 23, 11628–11640. https://doi.org/10.1523/JNEUROSCI.23-37-11628.2003
17. Fozzard, H.A., Sheets, M.F., Hanck, D., 2011. The Sodium Channel as a Target for Local Anesthetic Drugs. Front. Pharmacol. 2. https://doi.org/10.3389/fphar.2011.00068
18. Garrido, J.J., Giraud, P., Carlier, E., Fernandes, F., Moussif, A., Fache, M.-P., Debanne, D., Dargent, B., 2003. A targeting motif involved in sodium channel clustering at the axonal initial segment. Science 300, 2091–2094. https://doi.org/10.1126/science.1085167
19. Harrison, P.M., Badel, L., Wall, M.J., Richardson, M.J.E., 2015. Experimentally Verified Parameter Sets for Modelling Heterogeneous Neocortical Pyramidal-Cell Populations. PLOS Comput. Biol. 11, e1004165. https://doi.org/10.1371/journal.pcbi.1004165
20. Hill, E., Gowers, R., Richardson, M.J.E., Wall, M.J., 2021. α-Synuclein Aggregates Increase the Conductance of Substantia Nigra Dopamine Neurons, an Effect Partly Reversed by the KATP Channel Inhibitor Glibenclamide. eNeuro 8. https://doi.org/10.1523/ENEURO.0330-20.2020
21. Hill, E., Karikari, T.K., Moffat, K.G., Richardson, M.J.E., Wall, M.J., 2019. Introduction of Tau Oligomers into Cortical Neurons AltersAP Dynamics and Disrupts Synaptic Transmission and Plasticity. eneuro 6, ENEURO.0166-19.2019. https://doi.org/10.1523/ENEURO.0166-19.2019
22. Hill, E., Wall, M.J., Moffat, K.G., Karikari, T.K., 2020. Understanding the Pathophysiological Actions of Tau Oligomers: A Critical Review of Current Electrophysiological Approaches. Front. Mol. Neurosci. 13. https://doi.org/10.3389/fnmol.2020.00155
23. Hodgkin, A.L., Huxley, A.F., 1952. A quantitative description of membrane current and its application to conduction and excitation in nerve. J. Physiol. 117, 500–544.
24. Hoover, B.R., Reed, M.N., Su, J., Penrod, R.D., Kotilinek, L.A., Grant, M.K., Pitstick, R., Carlson, G.A., Lanier, L.M., Yuan, L.-L., Ashe, K.H., Liao, D., 2010. Tau mislocalization to dendritic spines mediates synaptic dysfunction independently of neurodegeneration. Neuron 68, 1067–1081. https://doi.org/10.1016/j.neuron.2010.11.030
25. Horowitz, P.M., LaPointe, N., Guillozet-Bongaarts, A.L., Berry, R.W., Binder, L.I., 2006. N-terminal fragments of tau inhibit full-length tau polymerization in vitro. Biochemistry 45, 12859–12866. https://doi.org/10.1021/bi061325g
26. Karikari, T.K., Keeling, S., Hill, E., Lantero Rodríguez, J., Nagel, D.A., Becker, B., Höglund, K., Zetterberg, H., Blennow, K., Hill, E.J., Moffat, K.G., 2020. Extensive Plasmid Library to Prepare

Tau Protein Variants and Study Their Functional Biochemistry. ACS Chem. Neurosci. 11, 3117–3129. https://doi.org/10.1021/acschemneuro.0c00469

27. Karikari, T.K., Nagel, D.A., Grainger, A., Clarke-Bland, C., Crowe, J., Hill, E.J., Moffat, K.G., 2019a. Distinct Conformations, Aggregation and Cellular Internalization of Different Tau Strains. Front. Cell. Neurosci. 13. https://doi.org/10.3389/fncel.2019.00296
28. Karikari, T.K., Nagel, D.A., Grainger, A., Clarke-Bland, C., Hill, E.J., Moffat, K.G., 2019b. Preparation of stable tau oligomers for cellular and biochemical studies. Anal. Biochem. 566, 67–74. https://doi.org/10.1016/j.ab.2018.10.013
29. Kaufmann, T.J., Harrison, P.M., Richardson, M.J.E., Pinheiro, T.J.T., Wall, M.J., 2016. Intracellular soluble α-synuclein oligomers reduce pyramidal cell excitability. J. Physiol. 594, 2751–2772. https://doi.org/10.1113/JP271968
30. Kole, M.H.P., Ilschner, S.U., Kampa, B.M., Williams, S.R., Ruben, P.C., Stuart, G.J., 2008.AP generation requires a high sodium channel density in the axon initial segment. Nat. Neurosci. 11, 178–186. https://doi.org/10.1038/nn2040
31. Kontis, K.J., Rounaghi, A., Goldin, A.L., 1997. Sodium Channel Activation Gating Is Affected by Substitutions of Voltage Sensor Positive Charges in All Four Domains. J. Gen. Physiol. 110, 391–401.
32. Köpke, E., Tung, Y.C., Shaikh, S., Alonso, A.C., Iqbal, K., Grundke-Iqbal, I., 1993. Microtubule-associated protein tau. Abnormal phosphorylation of a non-paired helical filament pool in Alzheimer disease. J. Biol. Chem. 268, 24374–24384. https://doi.org/10.1016/S0021-9258(20)80536-5
33. Lapointe, N.E., Horowitz, P.M., Guillozet-Bongaarts, A.L., Silva, A., Andreadis, A., Binder, L.I., 2009. Tau 6D and 6P isoforms inhibit polymerization of full-length tau in vitro. Biochemistry 48, 12290–12297. https://doi.org/10.1021/bi901304u
34. Lorincz, A., Nusser, Z., 2010. Molecular Identity of Dendritic Voltage-Gated Sodium Channels. Science 328, 906–909. https://doi.org/10.1126/science.1187958
35. Maeda, S., Sahara, N., Saito, Y., Murayama, S., Ikai, A., Takashima, A., 2006. Increased levels of granular tau oligomers: an early sign of brain aging and Alzheimer's disease. Neurosci. Res. 54, 197–201. https://doi.org/10.1016/j.neures.2005.11.009
36. Milescu, L.S., Bean, B.P., Smith, J.C., 2010. Isolation of somatic Na+ currents by selective inactivation of axonal channels with a voltage prepulse. J. Neurosci. Off. J. Soc. Neurosci. 30, 7740–7748. https://doi.org/10.1523/JNEUROSCI.6136-09.2010
37. Mondragón-Rodríguez, S., Salas-Gallardo, A., González-Pereyra, P., Macías, M., Ordaz, B., Peña-Ortega, F., Aguilar-Vázquez, A., Orta-Salazar, E., Díaz-Cintra, S., Perry, G., Williams, S., 2018. Phosphorylation of Tau protein correlates with changes in hippocampal theta oscillations and reduces hippocampal excitability in Alzheimer's model. J. Biol. Chem. 293, 8462–8472. https://doi.org/10.1074/jbc.RA117.001187
38. Ondrejcak, T., Klyubin, I., Corbett, G.T., Fraser, G., Hong, W., Mably, A.J., Gardener, M., Hammersley, J., Perkinton, M.S., Billinton, A., Walsh, D.M., Rowan, M.J., 2018. Cellular Prion Protein Mediates the Disruption of Hippocampal Synaptic Plasticity by Soluble Tau In Vivo. J.

Neurosci. Off. J. Soc. Neurosci. 38, 10595–10606. https://doi.org/10.1523/JNEUROSCI.1700-18.2018

39. Puopolo, M., Raviola, E., Bean, B.P., 2007. Roles of Subthreshold Calcium Current and Sodium Current in Spontaneous Firing of Mouse Midbrain Dopamine Neurons. J. Neurosci. 27, 645–656. https://doi.org/10.1523/JNEUROSCI.4341-06.2007
40. Puzzo, D., Piacentini, R., Fá, M., Gulisano, W., Li Puma, D.D., Staniszewski, A., Zhang, H., Tropea, M.R., Cocco, S., Palmeri, A., Fraser, P., D'Adamio, L., Grassi, C., Arancio, O., 2017. LTP and memory impairment caused by extracellular Aβ and Tau oligomers is APP-dependent. eLife 6. https://doi.org/10.7554/eLife.26991
41. Rademakers, R., Neumann, M., Mackenzie, I.R., 2012. Advances in understanding the molecular basis of frontotemporal dementia. Nat. Rev. Neurol. 8, 423–434. https://doi.org/10.1038/nrneurol.2012.117
42. Rall, W., Segev, I., 1985. Space-Clamp Problems When Voltage Clamping Branched Neurons With Intracellular Microelectrodes, in: Smith, T.G., Lecar, H., Redman, S.J., Gage, P.W. (Eds.), Voltage and Patch Clamping with Microelectrodes. Springer, New York, NY, pp. 191–215. https://doi.org/10.1007/978-1-4614-7601-6_9
43. Royeck, M., Horstmann, M.-T., Remy, S., Reitze, M., Yaari, Y., Beck, H., 2008. Role of Axonal NaV1.6 Sodium Channels inAP Initiation of CA1 Pyramidal Neurons. J. Neurophysiol. 100, 2361–2380. https://doi.org/10.1152/jn.90332.2008
44. Spruston, N., Jaffe, D.B., Williams, S.H., Johnston, D., 1993. Voltage- and space-clamp errors associated with the measurement of electrotonically remote synaptic events. J. Neurophysiol. 70, 781–802. https://doi.org/10.1152/jn.1993.70.2.781
45. Stuart, G., Schiller, J., Sakmann, B., 1997.AP initiation and propagation in rat neocortical pyramidal neurons. J. Physiol. 505, 617–632. https://doi.org/10.1111/j.1469-7793.1997.617ba.x
46. Tracy, T.E., Gan, L., 2018. Tau-mediated synaptic and neuronal dysfunction in neurodegenerative disease. Curr. Opin. Neurobiol. 51, 134–138. https://doi.org/10.1016/j.conb.2018.04.027
47. Uhlenbeck, G.E., Ornstein, L.S., 1930. On the Theory of the Brownian Motion. Phys. Rev. 36, 823–841. https://doi.org/10.1103/PhysRev.36.823
48. Van Wart, A., Trimmer, J.S., Matthews, G., 2007. Polarized distribution of ion channels within microdomains of the axon initial segment. J. Comp. Neurol. 500, 339–352. https://doi.org/10.1002/cne.21173
49. Yoshiyama, Y., Higuchi, M., Zhang, B., Huang, S.-M., Iwata, N., Saido, T.C., Maeda, J., Suhara, T., Trojanowski, J.Q., Lee, V.M.-Y., 2007. Synapse loss and microglial activation precede tangles in a P301S tauopathy mouse model. Neuron 53, 337–351. https://doi.org/10.1016/j.neuron.2007.01.010
50. Zhou, L., McInnes, J., Wierda, K., Holt, M., Herrmann, A.G., Jackson, R.J., Wang, Y.-C., Swerts, J., Beyens, J., Miskiewicz, K., Vilain, S., Dewachter, I., Moechars, D., De Strooper, B., Spires-Jones, T.L., De Wit, J., Verstreken, P., 2017. Tau association with synaptic vesicles

causes presynaptic dysfunction. Nat. Commun. 8, 15295. https://doi.org/10.1038/ncomms15295

Materials and Methods

Recombinant production of FL and tau fragments

Constructs: FL tau (amino acids 1-441 of tau 2N4R; Uniprot ID P10636-8), as well as the amino acids 1-123 (C^{FRAG}) and 124-441 (N^{FRAG}) variants of this protein were recombinantly produced in *E. coli.* The different fragments were PCR amplified using custom designed primers representing the 5' and 3' sequence respectively with Tau cDNA (RC213312, Origene) as template. The PCR fragment was cloned directly into pET_SUMO, a 6XHis tag and SUMO protein expression plasmid (Invitrogen), with a TA cloning site. Constructs were sequenced and transformed into E. coli BL21 (DE3) for expression.

SUMO fusion protein expression: E.coli BL21 (DE3) containing the sequence-confirmed plasmid constructs were incubated overnight in 20 ml Luria Bertani media with Kanamycin at a concentration of 50 µg/ml. The next morning, the turbid culture was used to inoculate 1L of Luria Bertani media with Kanamycin (50 µg/ml) at +37°C and when OD600 reached 0.5-0.7, protein expression was induced with 1.0 mM IPTG o/n at +26-28°C. BL21 (DE3) cells overexpressing tau forms were harvested by centrifugation at 7000 rpm for 20' at +4°C and the pellet stored at -20°C.

Purification: The pellet was resuspended in 5ml lysis buffer (20 mM Tris, 150 mM NaCl, 1% NP40 pH 7.5, plus a tablet of protease inhibitor cocktail from Roche) per mg of cell pellet and incubated at room temperature for 30 min. The lysate was centrifuged for 20 min at 17,000×*g*, 4 °C and the supernatant collected. The protein extract was added to Ni-NTA agarose (Novex) equilibrated with 10 mM imidazole in 1x Native buffer and incubated with rotation at +4°C for 1h. Ni-NTA agarose was washed with 1x Native buffer + 20 mM imidazole and 6xHis-SUMO-tau fusion protein was eluted with 250 mM imidazole in 1x Native buffer. Purified fusion protein was dialysed against 50 mM Tris, 150 mM NaCl, pH 8.0 and protein concentration was determined with BCA.

SUMO-tau fusion protein (2 mg) was cleaved by +4°C overnight incubation in 50 µg SENP-1 SUMO protease in 50 mM Tris, 150 mM NaCl, 1 mM DTT. After cleavage, 6xHis-tag and His-tagged SUMO protease was bound to Ni-NTA agarose, the flowthrough containing tag-free tau was collected and any residual bound Tau protein was eluted with imidazole gradient, starting at 20 mM. Fractions containing Tau protein were collected and dialyzed against PBS. If needed, protein was concentrated using AmiconUltra4. Polishing of the tag-free tau protein variants to remove truncates and aggregates was performed by size exclusion chromatography as described in Karikari et al., (2020b). We used a Superdex S200 10/300 GL column (GE Healthcare) running on an Ethan LC system (GE Healthcare), with the running buffer being 1× PBS pH 7.4 (2x PBS for tau1-123). The following molecular weight markers from Sigma (#MWGF70-1KT) were used to estimate the elution volumes of the proteins of interest: blue dextran (2000 kDa; void volume), bovine serum albumin (66 kDa), carbonic anhydrase (29 kDa), cytochrome C (12.4 kDa), and aprotinin (6.5 kDa). Each tau variant was purified in a two-step

process; 1ml fractions from the first size exclusion chromatography were analysed by gel chromatography followed by Western blotting with specific tau antibodies to select high-protein fractions for further processing. Selected high-yield fractions were pooled and concentrated using ultrafiltration devices of appropriate molecular weight cut-offs from Amicon as described in Karikari et al., (2020) .

Preparation of tau oligomers

To ensure the use of equal concentrations of the tau variants, molar concentrations were estimated using molecular weights specific to each tau construct sequence. Oligomers were prepared by overnight incubation of identical concentrations of each protein construct in 1X PBS at room temperature without shaking, a method validated (Karikari et al., 2019b). Monomers were treated similarly but were incubated at 4 ˚C overnight. The samples were immediately dry-frozen by dipping into dry ice mixed with ethanol and stored at -80 ˚C until use. Oligomer concentrations were expressed in equivalence of starting monomer concentrations. Unless otherwise stated, aggregates were introduced at 444 nM (based on monomeric MW).

Transmission electron microscopy

Formvar/carbon-coated 300-mesh copper grids (#S162, Agar Scientific) were glow-discharged using the ELMO system from Cordouan Technologies. Five microliters of labelled or unlabelled soluble tau aggregate preparations were pipetted onto the grid and allowed to bind for 1 min. Excess samples were removed with a strip of filter paper, and 5 µl of 2% uranyl acetate added for 1 min. After removing the excess stain with a strip of filter paper, the grids were imaged using a JEOL-2100F transmission electron microscope.

Electrophysiology

Preparation of hippocampal brain slices

All experiments were approved by the local Animals Welfare and Ethics Board (AWERB) at Authors University. C57/BL6 male mice (3-4 weeks of age) were killed by cervical dislocation and decapitated in accordance with the United Kingdom Animals (Scientific Procedures) Act (1986). Parasagittal hippocampal slices (350 µM) were cut with a Microm HM 650V microslicer in cold (2–4°C) high Mg^{2+}, low Ca^{2+} aCSF (artificial CSF), composed of the following: 127 mM NaCl, 1.9 mM KCl, 8 mM $MgCl_2$, 0.5 mM $CaCl_2$, 1.2 mM KH_2PO_4, 26 mM $NaHCO_3$, and 10 mM D-glucose (pH 7.4 when bubbled with 95% O2 and 5% CO_2, 300 mOsm). Following preparation, slices were left to recover in recording aCSF (as above but with 1 mM $MgCl_2$ and 2 mM $CaCl_2$) at 34°C. Slices were used within 1-8 hours after preparation.

Whole-cell patch clamp recording from pyramidal cells

A slice was transferred to the recording chamber, submerged and perfused (2–3 ml/min^{-1}) with aCSF at 30 °C. Slices were visualized using IR-DIC optics with an Olympus BX151W microscope (Scientifica) and a CCD camera (Hitachi). Whole-cell current-clamp recordings were made from pyramidal cells in area CA1 of the hippocampus using patch pipettes (5–10 MΩ) manufactured from thick-walled glass (Harvard Apparatus). Pyramidal cells were identified by their position in the slice, morphology (from

fluorescence imaging) and characteristics of the standard current−voltage relationship. Voltage recordings were made using an Axon Multiclamp 700B amplifier (Molecular Devices) and digitized at 20 kHz. Data acquisition and analysis were performed using pClamp 10 (Molecular Devices). Recordings from neurons that had a resting membrane potential of between –60 and –75 mV at whole-cell breakthrough were accepted for analysis. The bridge balance was monitored throughout the experiments and any recordings where it changed by > 20 % were discarded. Soluble tau aggregates were added to intracellular solution containing the following: 135 mM potassium gluconate, 7 mM NaCl, 10 mM HEPES, 0.5 mM EGTA, 10 mM phosphocreatine, 2 mM MgATP and 0.3 mM NaGTP (293 mOsm, pH 7.2) to give a final concentration of 444 nM (20 µg/ml tau). Intracellular solution was always filtered before adding tau aggregates to avoid any loss of tau in the filter.

Stimulation protocols

To extract the electrophysiological properties of recorded neurons, both step, ramp and more naturalistic, fluctuating currents were injected at 10-min intervals for a duration of the recordings as in (Hill et al., 2021, 2019; Kaufmann et al., 2016).

Standard IV protocol

The standard current−voltage relationship was constructed by injecting step currents from –200 pA incrementing by either 50 or 100 pA (1 s) until a regular firing pattern was induced. A plot of step current against voltage response around the resting potential was used to measure the input resistance (gradient of the fitted line).

Rheobase ramp protocol

To evaluate the rheobase (minimum current needed to elicit an action potential; AP) a current ramp was injected into neurons. From the baseline, a 100 ms ramp down by -50 pA, followed by a 900 ms ramp up by 150 pA, then a step back down to baseline.

Dynamic IV protocol

The dynamic IV curve, defined by the average transmembrane current as a function of voltage during naturalistic activity, can be used to efficiently parameterize neurons and generate reduced neural models that accurately mimic the cellular response. The method has been previously described (Badel et al., 2008a, 2008b; Harrison et al., 2015; Karikari et al., 2019b; Kaufmann et al., 2016), for the dynamic-IV computer code, see (Harrison et al., 2015). Briefly, a current wave form, designed to provoke naturalistic fluctuating voltages, was constructed using the summed numerical output of two Ornstein–Uhlenbeck processes (Uhlenbeck and Ornstein, 1930) with time constants τfast = 3 ms and τslow = 10 ms. This current wave form, which mimics the background post-synaptic activity resulting from activation of AMPA and $GABA_A$ receptor channels, is injected into cells and the resulting voltage recorded (a fluctuating, naturalistic trace). The firing rate was measured from voltage traces evoked by injecting a current wave form of the same gain for all recordings (firing rate ~2–3 Hz). APs were detected by a manually set threshold and the interval between APs measured.

The dynamic transmembrane current (I_{ion}) can be calculated using:

$$I_{ion}(V,t) + I_{noise} = I_{inj}(t) - C\frac{dV}{dt}$$

for which the injected current (I_{inj}) is known, the derivative (dV/dt) can be calculated from the experimentally measured voltage and the capacitance (C) is attained from a minimum variance procedure (Badel et al., 2008b). A scatter plot of the transmembrane current against voltage illustrates the dynamic relationship between the two, with the effects of weak background synaptic activity and other sources of high-frequency variability being accounted for as intrinsic noise (I_{noise}) (Badel et al., 2008b). Averaging the transmembrane current in 1 mV bins removes the time dependence of I_{ion} (V,t) to yield the typical ionic current and a particular voltage, and thus defines the dynamic I–V curve (I_{dyn}):

$$I_{dyn}(V) = Mean\,[I_{ion}(V,t)]$$

It is well established that the exponential integrate-and-fire model (Fourcaud-Trocmé et al., 2003) provides an excellent fit to the dynamic I-V curve (Badel et al., 2008b, 2008a; Harrison et al., 2015). The exponential integrate-and-fire (EIF) model is characterized by a voltage forcing term F(V) that is related to the I_{dyn} as:

$$F(V) = \frac{-I_{dyn}(V)}{C}$$

where the steady state forcing function F(V) for the EIF model is given as:

$$F(V) = \frac{1}{\tau}\left(E - V + \Delta_{\tau exp}\left(\frac{V - V_T}{\Delta_T}\right)\right) = -\frac{I_{dyn}(V)}{C}$$

The dynamic curve fitted to the EIF model was used to extract four parameters: membrane time constant (τ), resting potential (E), spike-initiation threshold (V_T) and spike-onset sharpness (Δ_T), which describes the voltage range over which an AP initiates (Badel et al., 2008a, 2008b; Harrison et al., 2015; Kaufmann et al., 2016). Dynamic *I–V* curves were constructed solely from the pre-spike voltage response (subthreshold and run up to spike) with all data falling within a 200 ms window after each spike being excluded from analysis.

Sodium channel current recordings

To record sodium channel currents in isolation, the intracellular and extracellular solutions used were modified from Milescu *et al*. (2010). The extracellular solution contained following (in mM): 124 NaCl, 25 $NaHCO_3$, 3 KCl, 1.5 $CoCl_2$, 1.0 $MgSO_4$, 0.5 NaH_2PO_4, and 30 D-glucose, equilibrated with 95% O_2 and 5% CO_2 (pH 7.4). Calcium chloride was replaced with cobalt chloride to block the voltage-gated calcium channel currents. Experiments were performed at room temperature (~ 22ºC to improve the quality of the voltage clamp, Milescu et al., 2010). To reduce the amplitude of the sodium channel currents, 50 mM Na^+ was present in the intracellular solution: 70 Cs-gluconate, 30 Na-gluconate, 10 TEA-Cl, 5 4-AP, 10 EGTA, 1 $CaCl_2$, 10 HEPES, 4 Mg-ATP, 0.3 Na_3-GTP, 10 Na_2-phosphocreatine. Series resistance (R_s) was measured throughout the recording and were typically in the range of 6-12 MΩ. Cells with R_s over 15 MΩ or those that differed by more than 20 % over the period of recording were discarded. R_s was not compensated, but the liquid junction potential of ~ 8 mV was corrected for. Leak currents were subtracted using the P/n protocol (1/4) and the resulting data displayed.

The stimulation protocol was adapted from (Milescu et al., 2010) to allow fully clamped somatic Na^+ channel currents to be recorded. Neurons were held at -80 mV. A depolarising pre-pulse was given (5

ms, -40 mV) to activate axonal, but not somatic, sodium channels. This was followed by a 1 ms step to -55 mV and then voltage steps (from -60 to 60 mV, 5 ms duration) were used to elicit controlled Na^+ channel current responses. The inter-sweep interval was 2 s. From the current responses, plots of current vs voltage or conductance vs voltage were calculated.

Conductance is given by the following equation:

$$Conductance\ (g) = I_{Na}/(V_{Step} - V_{Reversal})$$

The plot of conductance vs voltage was fitted with a Boltzmann equation:

$$y = \frac{A_1 - A_2}{1 + e^{(x-x_0)/dx}} + A_2$$

and then the half activation voltage and rate of activation constant were extracted and compared between control and oTau introduced neurons.

Hodgkin Huxley AP model

The Hodgkin-Huxley (HH; Hodgkin & Huxley, 1952) model is a simple but robust method for modelling the ionic conductance's that generate nerve APs. The HH model can be applied to study voltage gated sodium and potassium channels. It proposes that each sodium channel contains a set of 3 identical, rapidly responding, activation gates (the m-gates), and a single, slower-responding, inactivation gate (the h-gate) (Hodgkin & Huxley, 1952).

The membrane current is given by:

$$I = C_m \frac{dVm}{dt} + g_K(V_m - V_k) + g_{Na}(V_m - V_{Na}) + g_l(V_m - V_l)$$

Where I is the total membrane current and C_m is the membrane capacitance, g_K, g_{Na} and g_l are the potassium, sodium and leak conductance's per unit area, and V_k , V_{Na} and V_l are reversal potentials.

The sodium conductance can be given by:

$$I_{Na}(t) = \bar{g}_{Na} m(V_m)^3 h(V_m)(V_m - E_{Na})$$

Where $\bar{g}_{Na}$ is the maximal sodium conductance and *m* and *h* are quantities between 0 and 1 that are associated with sodium channel activation and inactivation, respectively. V_m is the membrane potential and E_{Na} is the reversal potential for sodium.

Initial parameters were assigned as follows: $\bar{g}_{Na}: 120\ mS/cm^2$, $\bar{g}_K: 36\ mS/cm^2$, $g_l: 0.3\ mS/cm^2$, $C_m: 1\ \mu F/cm^2$, $Vm: -70\ mV$, $E_{Na}: 60\ mV$, $E_K: -88\ mV$, $E_l: -54.4\ mV$ in line with Hodgkin and Huxley 1952)

All modelling was completed using either MATLAB or Julia software platforms (Bezanson et al., 2017).

Statistical analysis

Statistical analysis was performed using non-parametric methods: Kruskal–Wallis analysis of variance (ANOVA), Mann Whitney and Wilcoxon signed-rank tests as required for non-parametric data. All data

is represented as mean and standard error of the mean with individual experiments represented by single data points. Each recorded cell is one data point. All experimental conditions were measured using multiple animals, only 1 cell was recorded per slice and recording conditions were interleaved to remove bias introduced from individual animals. Data points for each experimental condition were derived from a minimum of 4 individual animals.

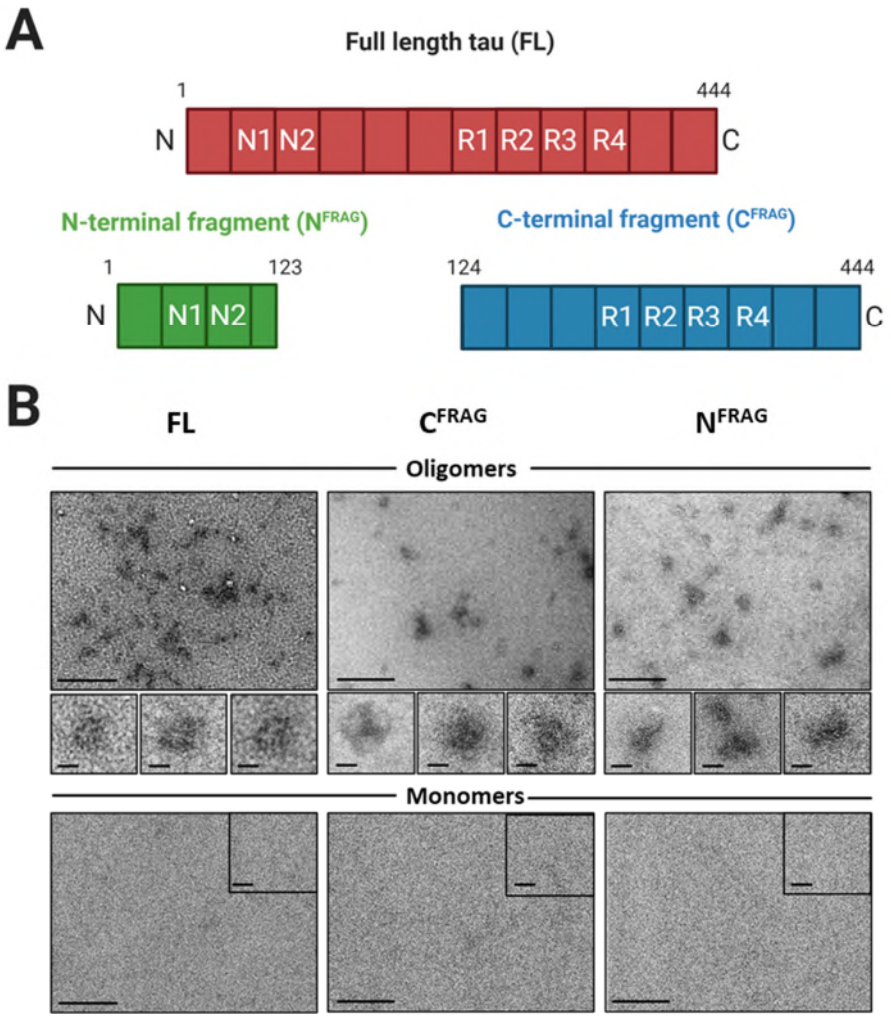

Figure 1: Structure and characterisation of the tau truncations.

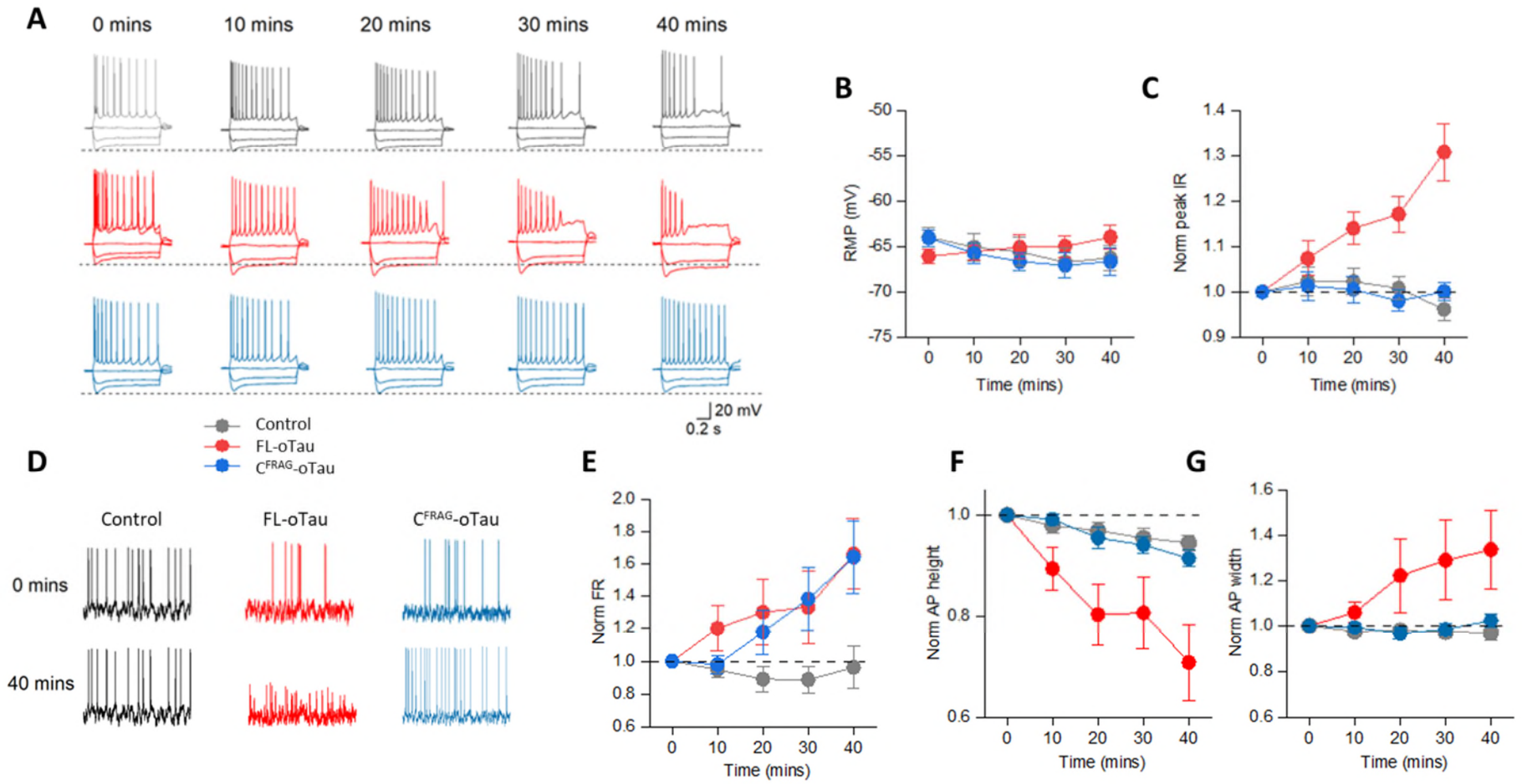

Figure 2: **The effects of FL-oTau on input resistance and AP waveform are abolished by N-terminal truncation, although the effects on excitability remain**

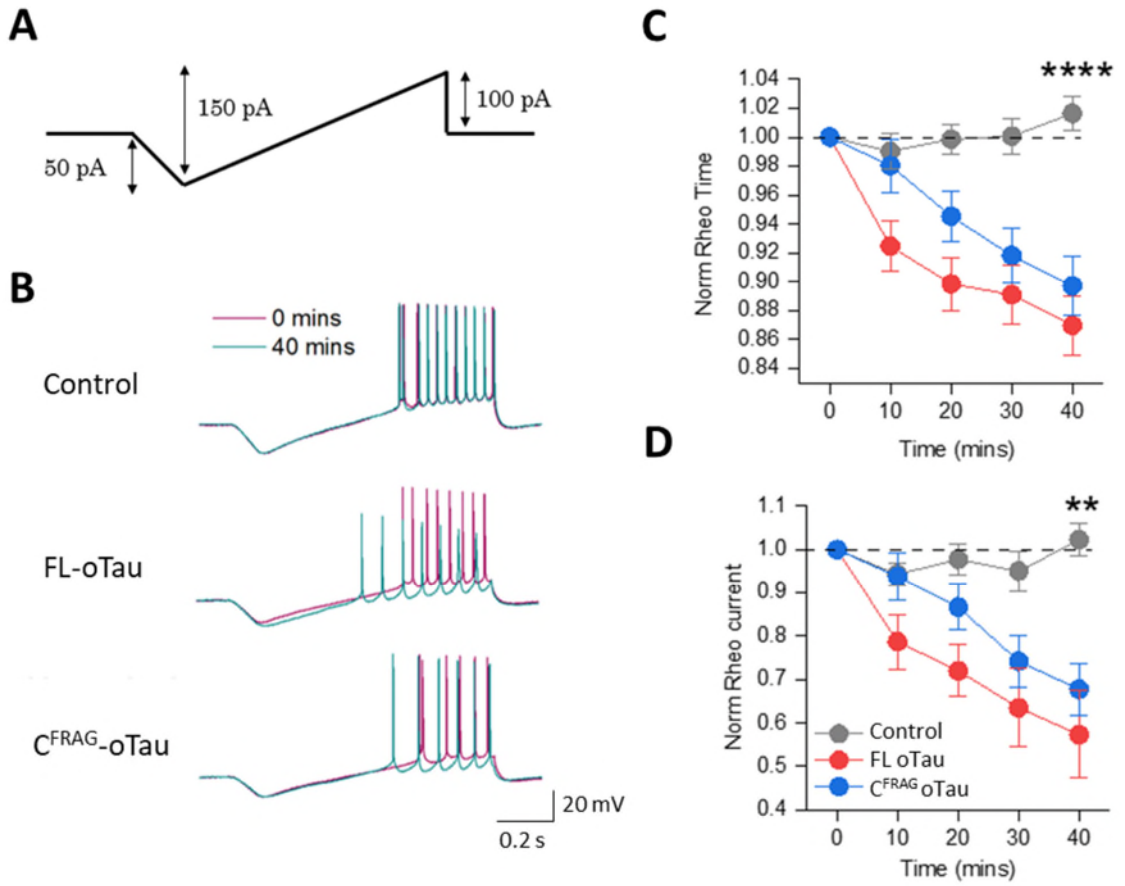

Figure 3: Protocol to investigate changes to the rheobase.

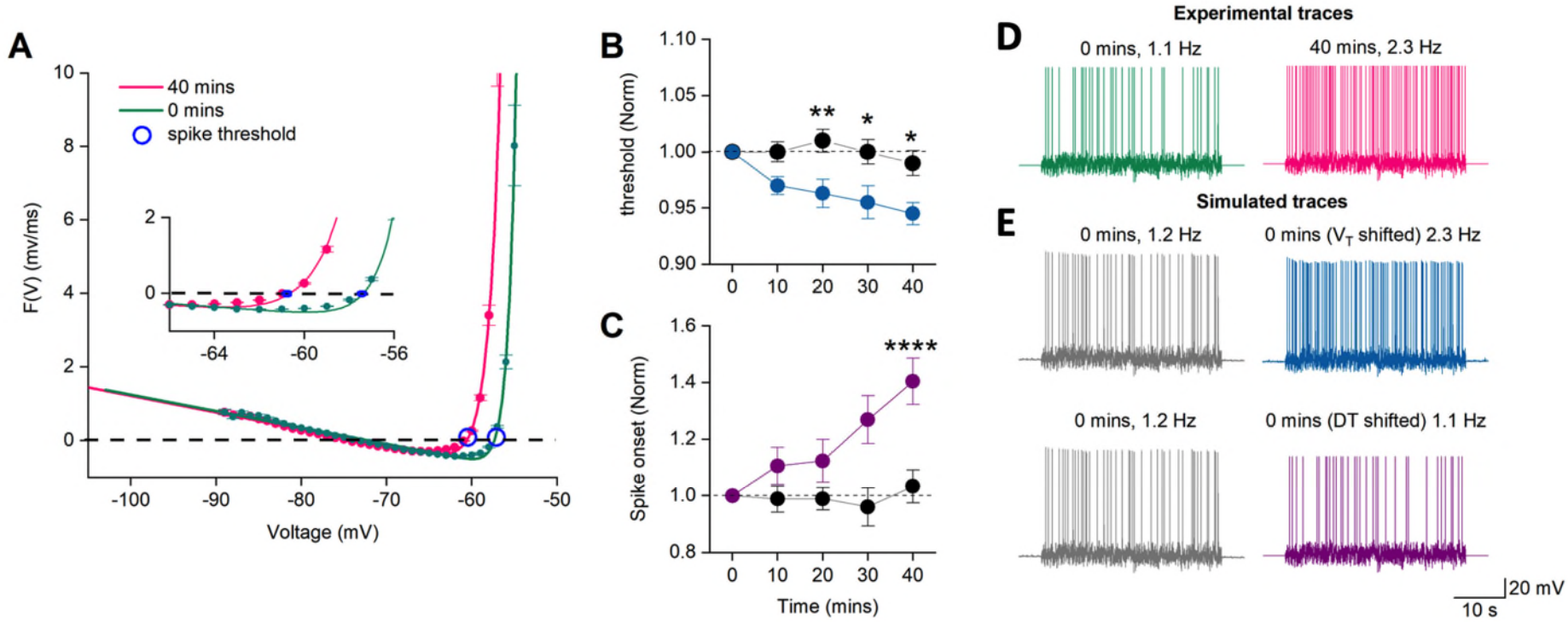

Figure 4: C^{FRAG} oTau-mediated shift in spike initiation threshold.

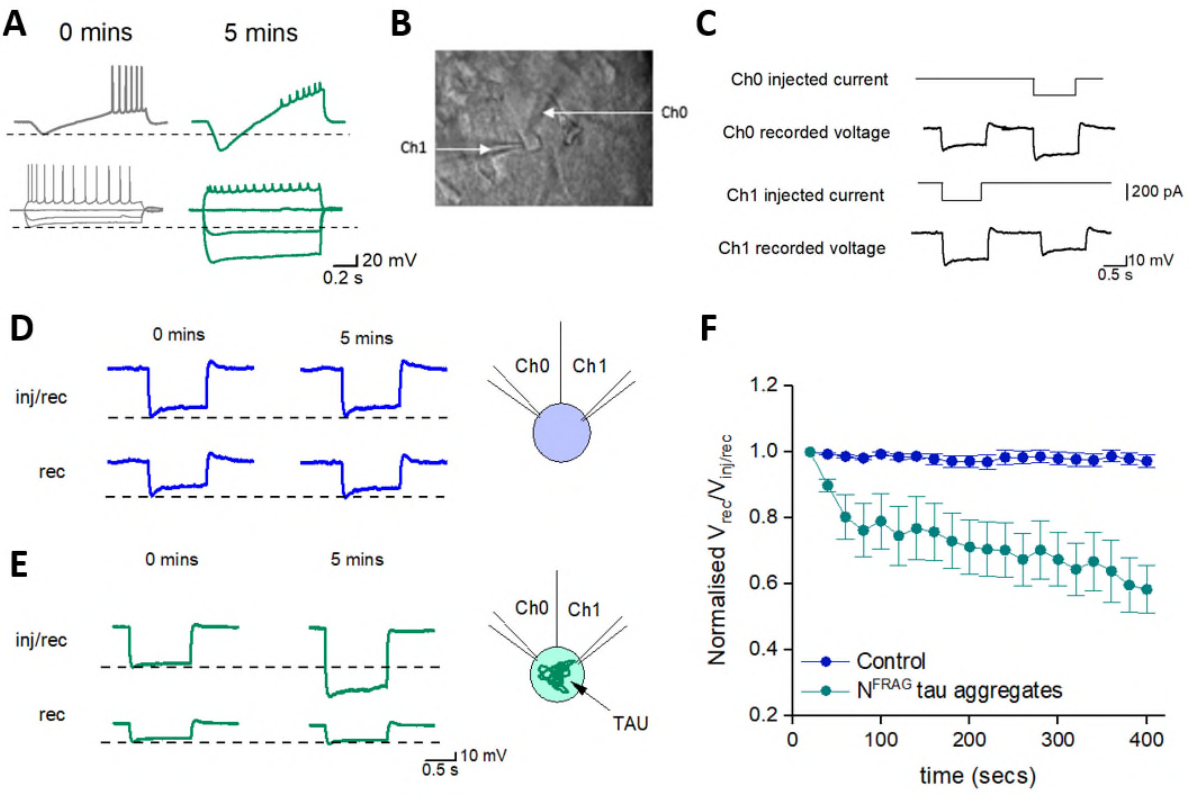

Figure 5: Rapid increase in input resistance mediated by 444 nM N^{FRAG} tau is due to aggregation in the soma impeding current flow.

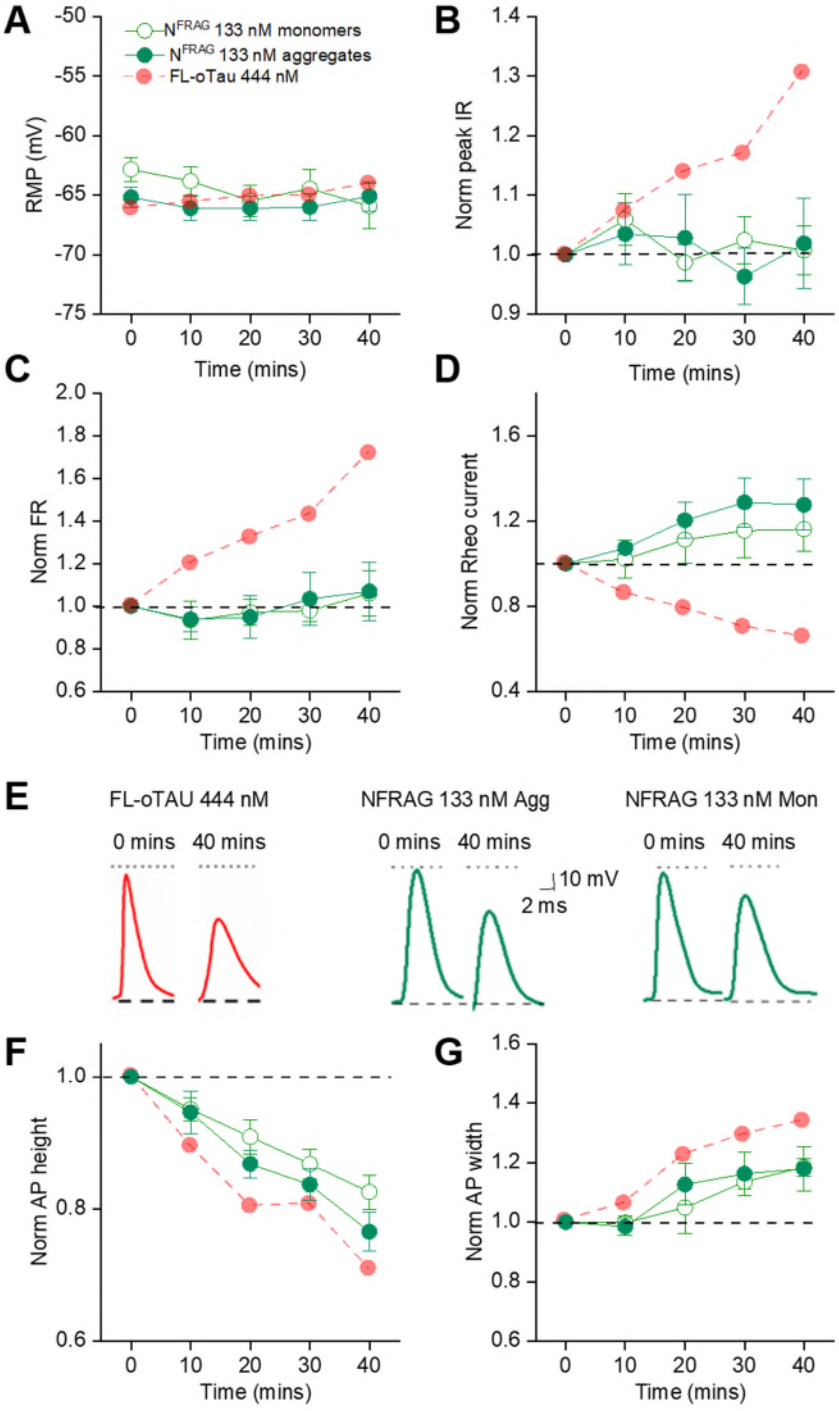

Figure 6: The effects of FL-oTau on action-potential waveform are maintained by N^{FRAG} aggregates and monomers.

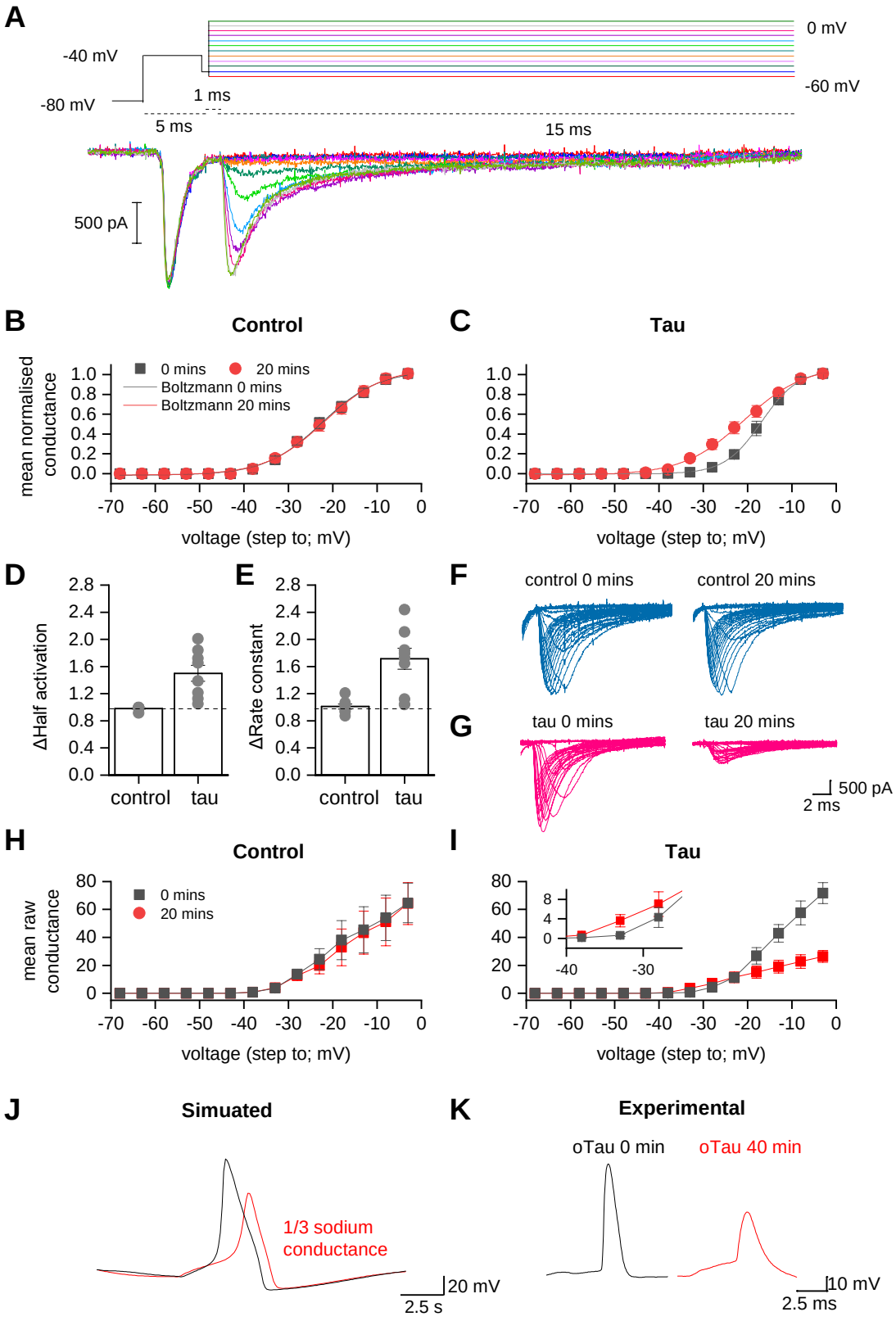

Figure 7: Tau directly modifies somatic sodium channel currents recorded from hippocampal CA1 neurons in acute slices

Figure 1: Structure and characterisation of the tau truncations. A) Schematic illustration of the recombinant tau constructs used in this study. Full length (FL) tau (441) has two N terminal repeat sequences (N1, N2) and four microtubule-binding pseudorepeat domains (R1–R4). Two trunctions were tested. The first, is an N-terminal truncated form of FL tau (termed C^{FRAG}) which consists of amino acids 124-444. The second, is the N-terminal fragment that is removed by the C^{FRAG} truncation (termed N^{FRAG}) which consists of amino acids 1-123, including both N-terminal repeat sequences. B) All three versions of tau (FL, C^{FRAG} and N^{FRAG}) were tested as monomers, and after undergoing the oligomerisation protocol. Top panels: Overnight incubation at room temperature in the absence of any aggregation inducer (*e.g.*, heparin) allowed each protein variant to form small, soluble tau aggregates, as monitored by negative-stain transmission electron microscopy. While FL and C^{FRAG} both formed granular oligomer-like aggregates, the N-terminal fragment polymerized into amorphous structures with no consistent shape. Insets: Higher magnification regions to highlight aggregate shape. Bottom panel: The monomer preparations did not form any visible aggregates. Scale bars = 200 nm and insets 20 nm.

Figure 2: **The effects of FL-oTau on input resistance and AP waveform are abolished by N-terminal truncation, although the effects on excitability remain.** A) Standard current−voltage response in control (vehicle) neurons (grey), FL tau (red) and C^{FRAG} tau (blue) over the 40-minute period of recording. In neurons with vehicle (control) introduced, there were no significant changes to any of the measured parameters over the 40-minute period of recording (0 vs 40 mins, peak input resistance $p = 0.1455$, firing rate $p = 0.1831$, AP amplitude $p = 0.0732$ or AP width $p = 0.2266$). B) Graph showing no change to the RMP over the period of recording for any of the experimental conditions (vehicle, FL oTau and C^{FRAG} oTau, $p = 0.0898$, 0.0859 and 0.0801 respectively). C) Graph plotting Rin against time. FL tau significantly increased input resistance (at 40 mins, Rin was increased to 130 ± 6.3 % of the resistance at time 0, whole cell breakthrough, $p = 0.0005$) whereas control neurons and neurons with C^{FRAG} tau showed no significant changes (at 40 mins, the Rin was 100 ± 2.1 % of the resistance at time 0, $p = 0.9263$). D) Example membrane-potential responses to naturalistic current injection at time 0 (after whole-cell breakthrough, top) and after 40 min of recording for each of the three conditions (vehicle, FL tau and C^{FRAG} oTau). There is a reduction in AP amplitude with FL oTau, whereas C^{FRAG} oTau and vehicle have no effect (C^{FRAG} oTau: no change in AP amplitude (at 40 minutes 91 ± 1.6 % of that at time 0 minutes, $p= 0.0791$) or AP width (at 40 minutes 102 ± 3.0 % of that at time 0 minutes $p = 0.4746$; FL oTau: AP amplitude at 40 minutes significantly ($p= 0.001$) reduced to 70 ± 7.4 % of that at time 0 minutes and AP width at 40 minutes significantly ($p = 0.0352$) increased to 134 ± 17.2 % of that at time 0 minutes). E) Graph plotting normalised firing rate (to time 0) against time. Both FL and C^{FRAG} oTau oligomers produce a significant increase in neuronal excitability that is not seen in vehicle cells. (FL oTau: at 40 mins, the firing rate, measured from the voltage response to naturalistic current injection, was 171 ± 19.3 % of that at time 0, $p = 0.02$; C^{FRAG} oTau: at 40 mins, the firing rate was 164 ± 22.5 % of that at time 0, $p = 0.0132$). (F) Graph plotting AP amplitude against time and (G) AP width against time. A reduction in AP amplitude (F) and increase in width (G) are only produced by FL oTau and not by C^{FRAG} oTau or vehicle. *Action potential (AP), Firing rate (FR), Input resistance (IR), Resting membrane potential (RMP)*

Figure 3: Protocol to investigate changes to the rheobase. A) Schematic of the ramp protocol used to elicit APs. This protocol was run at 10-minute intervals. B) Examples from representative cells (control, full length, and C^{FRAG} oTau) demonstrating effects on rheobase over time. C, D) Graphs plotting mean and SEM for control (vehicle), full length and C^{FRAG} oTau on rheobase over time. There was no significant difference in the minimal current (rheobase) to evoke an AP in control vs FL or C^{FRAG} neurons at time 0 (whole-cell breakthrough) using a Kruskal-Wallis One-Way ANOVA (at 0 mins, the mean rheobase in control was 61 ± 3.47 pA, with FL the mean rheobase was 68 ± 5.39 pA and with C^{FRAG} the mean rheobase was 79 ± 7.74 pA, p = 0.1289). In control neurons, there was no significant difference in the rheobase current over the duration of the recording (at 40 minutes, the rheobase was 105 ± 3 % of the value at time 0 mins, p=0.0830, Table 1). Both full length and C^{FRAG} oTau significantly reduced both the time when first AP was evoked and the current needed to elicit an AP, reflecting the increase in excitability. For FL tau, at 40 minutes the rheobase was 66 ± 7 % of the value at time 0 mins (p = 0.0015). When C^{FRAG} tau was introduced, at 40 minutes the rheobase was 70 ± 5 % of the value at time 0 mins (p = 0.0005, Table 1, Figure 3). A non-parametric two-way ANOVA was then used to evaluate whether the shift in rheobase was dependent solely on the treatment condition, on the timescale of recording, or a combination of both. A significant effect of time (p <0.0001) and condition (vehicle or C^{FRAG} oTau; p < 0.0001) were observed to contribute to the alteration of rheobase as well as an interaction between the two (p <0.0001), with significance observed from the 20-minute time-point onwards (as determined by post-hoc analysis; 20 mins p = 0.0064, 30 mins p < 0.0001, 40 mins p < 0.0001).

Figure 4: oTau-mediated shift in spike initiation threshold. For the dynamic I-V protocol, a naturalistic current is injected into the cell and the voltage recorded is then used to extract a set of parameters (resting potential E, time constant τ, and spike-threshold voltage VT; see methods for more details). The second point where the DIV curve crosses 0 (mV/ms) represents the spike initiation threshold. A) Representative example of the dynamic IV curve for a neuron with the N-terminal truncation of tau introduced at 0 mins (green) and 40 mins (pink). A shift in spike initiation threshold of 4 mV (more negative) can be observed, thus the neurons are more excitable. B) The mean normalised spike threshold data is plotted against time (with SEM) to show the reduction in spike threshold in C^{FRAG} cells compared with cells where vehicle was introduced. Data was normalised to the spike initiation threshold at time 0 mins. There was no significant difference between the spike initiation threshold in control vs C^{FRAG} neurons at time 0 (whole-cell breakthrough), thus the recordings were comparable (mean threshold in control neurons was -53.82 ± 1.46 mV, *n* = 12, compared to the mean threshold in C^{FRAG} neurons which was -53.7 ± 1.64 mV, *n* = 12, p = 0.5185). In control neurons, there was no significant difference in spike threshold over the duration of the recording (at 40 minutes, the spike threshold was 101.3 ± 1.1 % of the value at time 0 mins, p = 0.4766). Whereas for neurons where C^{FRAG} was introduced, the spike initiation threshold was significantly reduced (more negative) at 40 minutes was compared to 0 minutes (at 40 minutes, the spike threshold was 94.5 ± 0.9 % of the value at time 0 mins, p = 0.0010). A non-parametric two-way ANOVA was then used to evaluate whether the shift in threshold was dependent solely on the treatment condition, on the timescale of recording, or a

combination of both. A significant effect of time (p=0.0129) and condition (vehicle or C^{FRAG} oTau; p=0.0001) were observed to contribute to the alteration of spike initiation threshold, with significance observed from the 20-minute timepoint onwards (as determined by post-hoc analysis; 20 mins p = 0.0081, 30 mins p = 0.0474, 40 mins p = 0.0201). C) Graph plotting spike onset against time.

There was an increase in spike onset observed in neurons where C^{FRAG} was introduced, reflecting faster spike generation after reaching threshold. There was no significant difference between the onset in control vs C^{FRAG} neurons at time 0 (whole-cell breakthrough), thus the recordings were comparable in quality and stability (mean spike onset in control neurons was 1.01 ± 0.09 mV, *n* = 12, compared to the mean threshold in C^{FRAG} neurons which was 0.98 ± 0.13 mV, *n* = 12, p = 0.1285). In control neurons, there was no significant difference in spike onset over the duration of the recording (at 40 minutes, the spike onset was 103.2 ± 5.7 % of the value at time 0 mins, p = 0.9102). Whereas for neurons where 444 nM aggregated C^{FRAG} tau was introduced, the onset was increased (steeper, reflecting increased excitability) at 40 minutes was compared to 0 minutes (at 40 minutes, the spike onset was 140.4 ± 8.2 % of the value at time 0 mins, p = 0.0015). A non-parametric two-way ANOVA was then used to evaluate whether the shift in spike onset was dependent solely on the treatment condition, on the timescale of recording, or an interaction between both. A significant effect of time (p = 0.0047) and condition (vehicle or C^{FRAG} oTau; p = 0.0001) were observed to contribute to the alteration of spike onset, with significance observed from the 30-minute time-point onwards (as determined by post-hoc analysis; 30 mins p = 0.0019, 40 mins p = 0.0001). An interaction effect between condition and time was also noted (p = 0.0152). (D) Membrane-potential responses to naturalistic current injection for the neuron modelled in (A) demonstrates the increase in neuronal excitability mediated by the introduction of C^{FRAG} tau oligomers. (E) Simulated membrane- potential response based on the extracted neuronal parameters at time 0 mins (left), using the refractory integrate and fire model. The neuronal firing rate matches the experimental trace well. The spike threshold was then manually shifted by -4 mV and the simulation re-run (right, blue), resulting in an increase in excitability, comparable with the experimental trace at 40 mins (D). The same procedure was performed, but only shifting spike onset and re-simulating with little effect on excitability or firing rate, thus confirming that the increase in excitability is predominantly mediated by a shift in spike threshold.

Fig 5: Rapid increase in input resistance mediated by 444 nM N^{FRAG} tau is due to aggregation in the soma impeding current flow. A) Representative examples of rheobase and SIV protocols at 0 mins (whole cell breakthrough) and after 5 mins, demonstrating a rapid, large increase in input resistance and reduction in spike amplitude. At 5 minutes, the input resistance was 169 ± 24.2 % of that at 0 minutes (whole cell breakthrough), the time constant was reduced to 77 ± 3.2 % of that at 0 minutes and this change in time constant reflected a change in whole-cell capacitance (by 5 minutes the capacitance was reduced to 53 ± 5.4 % of that at 0 minutes (*n* = 4). B) Bright-field image of a CA1 neuron in the hippocampus with two patch pipettes recording simultaneously from the soma. C) Schematic of the stimulation protocol used, a 200 pA hyperpolarising current step was applied to Ch0 or Ch1 in turn and the voltage response was recorded in both channels (Ch0 or Ch1). D) Representative example where both pipettes were filled with vehicle, there was no change to the relative amplitude of

the voltage responses between 0 mins (whole-cell breakthrough) and 5 mins (the relative response was 97 ± 1.7 % of the response at 0 minutes, p = 0.1484, *n* = 8). E) Representative example when 444 nM N^{FRAG} was introduced via the 'inject and record pipette', the same rapid increase in voltage response (as in A) was observed. This was not reflected by an increase in the amplitude of the voltage step as measured by the 'recording only' pipette, suggesting that the aggregates are impeding the flow of current between the pipettes (at 5 minutes the relative response was 58.4 ± 7 % of the response at 0 minutes, p = 0.0078, *n* = 8). F) Mean and SEM data for control (*n* = 8) and 444 nM N^{FRAG} recordings (n=8). A significant reduction in the voltage response measured by the 'record' pipette compared to the 'inject and record' pipette (where tau was introduced) can be observed. A non-parametric two-way ANOVA was also used to evaluate whether the resistance change was dependent solely on the treatment condition, on the timescale of recording, or a combination of both. A significant effect of time (p = 0.0489) and condition (vehicle or N^{FRAG}, p < 0.0001) were observed to contribute to the alteration resistance.

Figure 6: The effects of FL-oTau on action-potential waveform are maintained by N^{FRAG} aggregates and monomers. (A) Graph showing that there is no change to the RMP over the period of recording for any of the conditions. (N^{FRAG} tau aggregates: at 40 mins, the RMP was 99 ± 1.0 % of that at time 0, p = 0.9609, *n* = 12; N^{FRAG} tau monomers at 40 mins, the RMP was 104 ± 2.4 % of that at time 0, p = 0.0938, *n*=12). (B) Graph showing that there is no change to the input resistance over the period of recording for 133 nM N^{FRAG} aggregates or monomers (N^{FRAG} tau aggregates: at 40 mins, the peak input resistance, measured from the voltage response to step current injection, was 102 ± 7.7 % of that at time 0, p = 0.9531; N^{FRAG} tau monomers: at 40 mins, the peak input resistance, measured from the voltage response to step current injection, was 102 ± 4.1 % of that at time 0, p = 0.9395). (C) Graph showing that there is no change to firing rate over the period of recording for 133 nM N^{FRAG} aggregates or monomers. (N^{FRAG} tau aggregates: at 40 mins, the firing rate, measured from the voltage response to naturalistic current injection, was 107 ± 13.6 % of that at time 0, p = 0.7471; N^{FRAG} tau monomers: at 40 mins, the firing rate, measured from the voltage response to naturalistic current injection, was 106 ± 10.5 % of that at time 0, p = 0.5068). (D) Graph showing that there is no change to the rheobase current over the period of recording for 133 nM N^{FRAG} aggregates or monomers (N^{FRAG} tau aggregates: at 40 mins, the rheobase was 127 ± 11.9 % of that at time 0, p = 0.1294; N^{FRAG} tau monomers: at 40 mins, the rheobase was 116 ± 10.1 % of that at time 0, p = 0.2402). (E) Representative examples of AP waveforms for an individual neuron with one of the three conditions introduced (444 nM FL-oTau, 133 nM N^{FRAG} aggregates or monomers). A comparable effect on AP height and width is observed. (F) Graph showing that there is a comparable change to AP height over the period of recording for 133 nM N^{FRAG} aggregates or monomers and FL-oTau (N^{FRAG} tau aggregates: AP amplitude at 40 minutes was significantly reduced to 76 ± 2.9 % of that at time 0 minutes, p=0.0005; N^{FRAG} tau monomers: AP amplitude at 40 minutes was significantly reduced to 82 ± 2.6 % of that at time 0 minutes, p=0.0010). (G) Graph showing that there is a comparable change to AP width over the period of recording for 133 nM N^{FRAG} aggregates or monomers and FL-oTau. (N^{FRAG} tau aggregates: AP width at 40 minutes was significantly increased to 118 ± 7.4 % of that at time 0 minutes, p = 0.0186; N^{FRAG} tau

monomers: AP width at 40 minutes was significantly increased to 123 ± 2.0 % of that at time 0 minutes, p = 0.0303). *Pale red lines demonstrate the effects of FL-oTau for comparison (data presented in figure 2). Action potential (AP), Firing rate (FR), Input resistance (IR), Resting membrane potential (RMP).*

Figure 7: Tau directly modifies somatic sodium channel currents recorded from hippocampal CA1 neurons in acute slices. A) Example of the recording protocol (adapted from Milescu *et al*., 2010). A pre-pulse step of 5 ms from the holding value of -80 mV to -40 mV elicits a current response from axonal (but not somatic) sodium channels. There is a brief step to -55 mV (1 ms) before the steps used to evoke the controlled sodium channel currents (15 ms). The steps were given on consecutive sweeps from -60 V to + 60 mV (5 mV increment) with a 2 s gap between each sweep. Leak currents were subtracted with the P/N protocol (1/4) and the junction potential (+ 8 mV) was corrected for. B) Conductance was calculated using the following equation: conductance *(g) = current (I)/ (Vstep – Vreversal).* The conductance in response to steps up to 0 mV is plotted as a mean (and SEM) of all control cells (n=7). C) The conductance in response to steps up to 0 mV is plotted as a mean (and SEM) of all tau introduced cells (n = 7) is plotted. For B and C, the grey line is 0 mins and the red 20 mins. A Boltzmann fit allows half activation voltage and the time constant (measure of the speed of activation). D) Mean change from 0 mins to 20 mins for control and tau cells in half activation, data is given relative to the value at time 0. Mean and SEM are shown, and individual data points are overlaid on top. While control cells are stable over 20 mins (at 20 mins, the half activation was 98 ± 1.0 % of that at time 0, p = 0.2031), FL-oTau introduced cells see a significant decrease in half activation (activate at lower voltages; increase in excitability), at 20 minutes, the half activation was 150 ± 11.7 % of that at time 0, p = 0.0078. We also see a doubling of the rate constant of activation (E). In control cells, at 20 mins, it was 101 ± 3.6 % of that at time 0, p = 0.9375, whereas in FL-oTau introduced neurons had increased significantly to 171 ± 15.4 % of that at time 0, p = 0.0078. F, G) Representative example current sodium current recordings for control and FL-oTau at 0 mins and 20 mins demonstrating the reduction in peak current induced by FL oTau. H, I) Raw conductance data (averaged) to highlight the reduction in maximal conductance for FL-oTau after 20 mins. Inset demonstrates the crossover at low voltages, where FL oTau at 20 mins has higher conductance, despite the maximal conductance being reduced at higher voltages. J) Implementing a simple Hodgkin Huxley model of action-potential dynamics to predict the effect of reducing the maximal sodium conductance by 2/3 (as measured experimentally (I)). The simulated reduction in current amplitude and rise to threshold appears to match the experimental phenotype for FL-oTau (J).

	Vehicle/ control (n=12)				Full length tau (n=12)				C^{FRAG} (n=12)			
	0 mins		40 mins		0 mins		40 mins		0 mins		40 mins	
Parameter	**Mean**	**SEM**	**Mean**	**SEM**	**Mean**	**SEM**	**Mean**	**SD**	**Mean**	**SEM**	**Mean**	**SEM**
RMP (mV)	-64	± 1.07	-66	± 1.36	-66	± 0.75	-64	± 1.30	-64	± 0.92	-67	± 1.52
Peak Rin (MΩ)	204	± 18.6	197	± 20.1	165	± 6.29	218	± 16.1	178	± 13.4	177	± 11.7
Firing Rate (Hz)	1.73	± 0.4	1.63	± 0.45	1.25	± 0.3	1.73	± 0.3	1.1	± 0.19	1.5	± 0.21
AP Height (mV)	85	± 2.52	83	± 2.86	87	± 3.42	63	± 7.48	89	± 2.19	86	± 2.45
AP width (ms)	1.8	± 0.09	1.7	± 0.08	1.8	± 0.05	2.4	± 0.34	1.8	± 0.06	1.9	± 0.06
Rheobase (pA)	61	± 3.47	60	± 4.51	68	± 5.39	47	± 7.42	79	± 7.74	56	± 8.18

Table 1: Electrophysiological parameters measured for dopaminergic neurons at time zero and time 40 mins for each experimental treatment (vehicle, FL-oTau, and C^{FRAG} o-Tau. Data is displayed as mean and SEM of the raw values. Action potential (AP), Firing rate (FR), Input resistance (IR), Resting membrane potential (RMP). There was no significant difference in the electrophysiological parameters at time 0 (whole-cell breakthrough) across the three conditions. (Kruskal-Wallis One-Way ANOVAs resting potential p = 0.1386, peak input resistance p = 0.2288, firing rate p = 0.6439, action potential (AP) amplitude p = 0.7528 or AP width p = 0.9090, n = 12 for each condition).

Findings	FL- oTau (444 nM)	C^{FRAG} -oTau (444 nM)	N^{FRAG}-oTau (444 nM)	N^{FRAG}-oTau (133 nM)	N^{FRAG}-Tau (133 nM)	Potential mechanism
AP amplitude	↓	-	↓	↓	↓	Slower activation of voltage-gated sodium channels
AP width	↑	-	↑	↑	↑	
Input resistance	↑	-	↑	-	-	Aggregation in the soma impeding current flow, lowering apparent capacitance.
Firing rate	↑	↑	-	-	-	Hyperpolarised shift in spike initiation threshold. Shift in the half activation of voltage-gated sodium channels
Rheobase	↓	↓	-	-	-	

Table 2: Summary of findings using recombinant truncations of tau and identified mechanisms.